Ocean Modelling 40 (2011) 72–86

Contents lists available at ScienceDirect

Ocean Modelling

journal homepage: www.elsevier.com/locate/ocemod

Physical vs. numerical dispersion in nonhydrostatic ocean modeling

Sean Vitousek *, Oliver B. Fringer

Environmental Fluid Mechanics Laboratory, Stanford University, Stanford, CA 94305, United States

ARTICLE INFO

Article history:
Received 11 September 2010
Received in revised form 29 May 2011
Accepted 1 July 2011
Available online 14 July 2011

Keywords:
Dispersion
Nonhydrostatic effects
Internal waves
Ocean modeling
Grid resolution requirements
Leptic ratio
Lepticity

ABSTRACT

Many large-scale simulations of internal waves are computed with ocean models solving the primitive (hydrostatic) equations. Under certain circumstances, however, internal waves can represent a dynamical balance between nonlinearity and nonhydrostasy (dispersion), and thus may require computationally expensive nonhydrostatic simulations to be well-resolved. Most discretizations of the primitive equations are second-order accurate, inducing numerical dispersion generated from odd-order terms in the truncation error (3rd-order derivatives and higher). This numerical dispersion mimics physical dispersion due to nonhydrostasy. In this paper, we determine the numerical dispersion coefficient associated with common discretizations of the primitive equations. We compare this coefficient to the physical dispersion coefficient from the Boussinesq equations or KdV equation. The results show that, to lowest order, the ratio of numerical to physical dispersion is $\Gamma = K\lambda^2$, where K is an $O(1)$ constant dependent on the discretization of the governing equations and λ is the grid leptic ratio, $\lambda \equiv \Delta x/h_1$, where Δx is the horizontal grid spacing and h_1 is the depth of the internal interface. In addition to deriving this relationship, we verify that it indeed holds in a nonhydrostatic ocean model (SUNTANS). To ensure relative dominance of physical over numerical effects, simulations require $\Gamma \ll 1$. Based on this condition, the horizontal grid spacing required for proper resolution of nonhydrostatic effects is $\lambda < O(1)$ or $\Delta x < h_1$. When this condition is not satisfied, numerical dispersion overwhelms physical dispersion, and modeled internal waves exist with a dynamical balance between nonlinearity and numerical dispersion. Satisfaction of this condition may be a significant additional resolution requirement beyond the current state-of-the-art in ocean modeling.

Published by Elsevier Ltd.

1. Introduction

Dispersion, a characteristic of nonlinear or nonhydrostatic waves, occurs when the wave speed is a non-constant function of the wave amplitude or wave frequency (or similarly wavelength) (Whitham, 1974). Distinction is sometimes made between these two types of dispersion, namely amplitude dispersion and frequency dispersion, respectively (LeBlond and Mysak, 1978). The two are synonymous with nonlinearity and nonhydrostasy in studies of gravity waves, and hence are typically called nonlinearity and dispersion.

Interesting wave phenomena exist when both nonlinearity and dispersion occur together and with approximately equal magnitude. Under such circumstances, nonlinear steepening balances dispersive spreading, and propagating waves of constant form known as "solitary" waves are possible (Korteweg and de-Vries, 1895). The most common equations satisfying the balanced motion include the Boussinesq equations (Boussinesq, 1871, 1872; Peregrine, 1967) and the Korteweg–de Vries (KdV) equation (Korteweg and de-Vries, 1895). These equations represent the depth-averaged conservation of mass and momentum and include dispersive effects due to nonhydrostasy by retaining the lowest-order effects of integrating the nonhydrostatic pressure over the depth. The KdV equation reduces conservation of mass and momentum to a single equation which is valid only for unidirectional wave propagation. In this paper, we rely heavily on the Boussinesq equations and KdV equation as models that faithfully represent nonlinear and nonhydrostatic behavior in more complicated natural systems, in this case, oceanic internal gravity waves.

Many researchers have relied on weakly nonlinear, weakly nonhydrostatic KdV theory to understand both qualitative and quantitative details of internal waves (Helfrich and Melville, 2006). Internal wave dynamics have been examined using the KdV framework which shows good comparison of internal wave profiles with the analytical result from the KdV equation (Liu et al., 1998; Stanton and Ostrovsky, 1998; Duda et al., 2004; Warn-Varnas et al., 2010). Developments extending KdV theory to fully nonlinear dynamics have made significant contributions to the literature, a complete list of which is given in Helfrich and Melville (2006). However, weakly nonlinear, weakly nonhydrostatic scaling of many internal wave problems justifies use of traditional KdV theory.

* Corresponding author.
E-mail addresses: seanv@stanford.edu (S. Vitousek), fringer@stanford.edu (O.B. Fringer).

1463-5003/$ - see front matter Published by Elsevier Ltd.
doi:10.1016/j.ocemod.2011.07.002

Many oceanic internal waves are long relative to the depth and hence are nearly hydrostatic. Therefore, modeling waves of such scale with a hydrostatic model may be appropriate (Kantha and Clayson, 2000). In many other cases, near continental shelves and ocean ridges, internal waves can be highly nonlinear and nonhydrostatic, often appearing as rank-ordered solitary-like wave trains (Hunkins and Fliegel, 1973; Apel et al., 1985; Liu et al., 1998; Scotti and Pineda, 2004). Thus, simulations of internal waves may require fully nonhydrostatic models (such as MITgcm (Marshall et al., 1997), SUNTANS (Fringer et al., 2006), nonhydrostatic ROMS (Kanarska et al., 2007)). The drawback of fully nonhydrostatic models is the computational cost associated with solving a 3-D elliptic equation for the nonhydrostatic pressure, which may require an order of magnitude increase in computational time (Fringer et al., 2006). The prohibitive computational cost requirement as well as the nearly hydrostatic scales make primitive (hydrostatic) ocean models the preferred method for simulating internal waves in the ocean. Although not as computationally expensive, the primitive equations do not resolve physical dispersion resulting from nonhydrostatic effects. However, this may not be a problem when physical dispersion is negligible. An excellent discussion concerning the application of hydrostatic models to the problem of simulating internal waves is presented in Hodges et al. (2006). They propose that future use of primitive ocean models is justified due to the clear hydrostatic scaling of most problems of interest. However, they also point out issues that modelers must contend with when simulating processes which include internal waves with hydrostatic models. As we will show, it is not only the lack of physical dispersion that adversely influences model results of internal waves, but the presence of numerical dispersion.

The concept of numerical dispersion is not particularly new. Long has it been known that even if the governing equations are nondispersive, their discrete model may be (artificially) dispersive (Trefethen, 1982). In early work, some authors referred to this as "spurious dispersion" (Vichnevetsky, 1980; Vichnevetsky and Bowles, 1982). Numerical dispersion generally refers to the class of essentially unavoidable spurious oscillations that result from numerical discretization. In other fields, particularly electrodynamics and acoustics, dispersion–relation–preserving numerical schemes (Tam and Webb, 1993) have received significant attention.

The effects of numerical dispersion have received limited attention in the literature on gravity waves. One instance is from Burwell et al. (2007), who examine the numerically diffusive and dispersive properties of tsunami models and find the horizontal grid resolution is critical to accurately simulate the dispersive behavior. They suggest a method, based on the concept in Shuto (1991), in which the grid resolution and thus the numerical dispersion can be tuned to replicate the physical dispersion not resolved in the (hydrostatic) model. Gottwald (2007) show that discretization of the inviscid Burgers equation can result in the KdV equation as its corresponding modified equivalent partial differential equation, where the (purely numerical) dispersive term is generated from truncation error. Schroeder and Schlünzen (2009) derive a numerical dispersion relation for an atmospheric internal gravity wave model. Their relation naturally tends toward the true dispersion relation as the horizontal grid spacing approaches zero. In simulations of internal waves, numerical dispersion is particularly adverse because it may create an artificial balance with the nonlinear steepening tendency of the wave and produce solitary-like waves that are physically unrealistic or impossible. Both Hodges et al. (2006) and Wadzuk and Hodges (2009) speculate that this is the problem with inconsistencies arising in hydrostatic ocean models. In this paper, we will demonstrate that this is indeed the case.

Numerical dispersion typically results from odd-ordered derivatives (3rd-order and higher) in the truncation error of finite-difference approximations to first-order derivatives in the governing equations. Often second-order central differences are used, implying that the dominant numerical dispersion coefficient is proportional to the horizontal grid spacing squared. In this paper, we determine the numerical dispersion coefficient from the modified equivalent partial differential equation given from a particular discretization (Hirt, 1968). Such analyses would be of limited use without, as a point of comparison, the physical dispersion coefficient. For internal waves, as mentioned previously, this is provided by the Boussinesq equations or the KdV equation. Realistic nonhydrostatic simulations require that the physical dispersion is much larger than the numerical dispersion. Because the physical dispersion for a given problem is typically fixed, the problem of minimizing numerical dispersion in nonhydrostatic ocean models reduces to the problem of providing adequate horizontal resolution. As we will show, this adequate horizontal resolution is $\Delta x < h_1$ where Δx is the horizontal grid spacing and h_1 is the depth of the internal interface.

The remainder of this paper is divided into four sections. Section 2 presents the governing equations for modeling dynamics of internal waves used in our analysis and derives the ratio of numerical to physical dispersion and associated resolution requirements of a model. Section 3 presents numerical simulations of the KdV equation and the fully nonhydrostatic ocean model SUNTANS and illustrates how both models are prone to numerical dispersion. Finally, Sections 4 and 5 present the discussion and conclusions of the methods in this paper, respectively.

2. Governing equations

We begin with the nondimensional two-layer Boussinesq equations representing the weakly nonlinear and weakly nonhydrostatic motion of the two-layer system depicted in Fig. 1. In this paper, we indicate nondimensional quantities with a $*$. Following Lynett and Liu (2002), the governing nondimensional momentum and continuity equations in one horizontal dimension which retain the first-order nonlinear and nonhydrostatic effects are given by

$$\frac{\partial U_1^*}{\partial t^*} + \delta U_1^* \frac{\partial U_1^*}{\partial x^*} + \frac{\partial \eta^*}{\partial x^*} - \epsilon^2 \frac{h_1^{*2}}{3} \frac{\partial^2}{\partial x^{*2}} \left(\frac{\partial U_1^*}{\partial t^*} \right) = O(\epsilon^2 \delta, \epsilon^4), \tag{1}$$

$$\frac{\partial \xi^*}{\partial t^*} - \frac{\partial}{\partial x^*} \left[(h_1^* - \delta \xi^*) U_1^* \right] = O(\Delta \rho^*), \tag{2}$$

$$\frac{\partial U_2^*}{\partial t^*} + \delta U_2^* \frac{\partial U_2^*}{\partial x^*} + \frac{1}{\rho_2^*} \frac{\partial}{\partial x^*} (\rho_1^* \eta^* + \xi^*) + \epsilon^2 \frac{h_2^{*2}}{6} \frac{\partial^2}{\partial x^{*2}} \left(\frac{\partial U_2^*}{\partial t^*} \right) - \epsilon^2 \frac{h_2^*}{2} \frac{\partial^2}{\partial x^{*2}} \left(h_2^* \frac{\partial U_2^*}{\partial t^*} \right) = O(\epsilon^2 \delta, \epsilon^4), \tag{3}$$

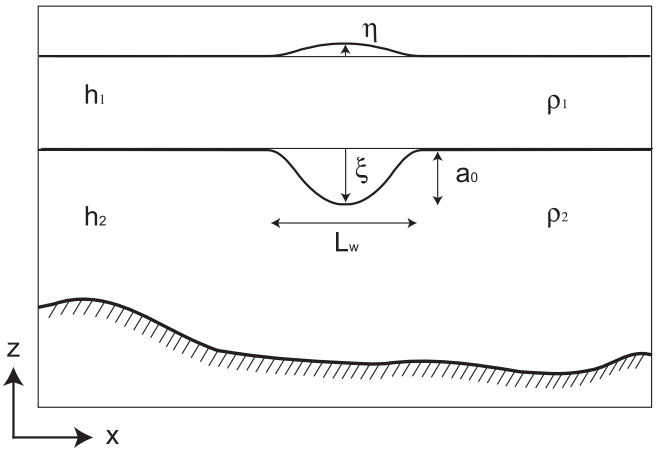

Fig. 1. Basic dimensional setup of the problem after Lynett and Liu (2002).

$$\frac{\partial \xi^*}{\partial t^*} + \frac{\partial}{\partial x^*}\left[(h_2^* + \delta\xi^*)U_2^*\right] = 0. \tag{4}$$

The nondimensional horizontal velocity in the upper and lower layers are given by $U_1^* = U_1/U_0$ and $U_2^* = U_2/U_0$, respectively, where U_0 is the characteristic flow velocity. The nondimensional densities of the upper and lower layers are given respectively by $\rho_1^* = \rho_1/\rho_0$ and $\rho_2^* = \rho_2/\rho_0$, where $\rho_2 > \rho_1$ and typically $\rho_0 = \rho_2$, and it is assumed that $\Delta\rho^* = (\rho_2 - \rho_1)/\rho_0 \ll 1$. The nondimensional height of the free surface above the still water level is $\eta^* = \eta/(a_0\Delta\rho^*)$, and $\xi^* = \xi/a_0$ is the nondimensional height of the internal interface above the still interface level and a_0 is a measure of the interface deflection. $h_1^* = h_1/h_0$ and $h_2^* = h_2/h_0$ are the nondimensional depths of the upper and lower layers, respectively, where the characteristic water depth is given by

$$h_0 = \frac{h_1 h_2}{h_1 + h_2}, \tag{5}$$

and h_1 and h_2 are the dimensional layer depths in quiescent conditions i.e. $\eta = \xi = 0$.

Two nondimensional parameters, δ and ϵ, play important roles in the behavior of the equations, since they represent the degree of nonlinearity and nonhydrostasy of the wave solutions, respectively. These parameters are given by

$$\delta = \frac{a_0}{h_0}, \tag{6}$$

$$\epsilon = \frac{h_0}{L_w}, \tag{7}$$

where L_w is the internal wave horizontal length scale. Eqs. (1) and (3) are derived under the assumptions of weak nonlinearity and weak nonhydrostasy, viz. $O(\delta) = O(\epsilon^2) < O(1)$. Thus the higher-order terms are $O(\delta^2) = O(\epsilon^4) \ll 1$ and therefore negligible.

In the following, we show that the two-layer Boussinesq equations, (1)–(4), under the assumption of a deep lower layer, can be reduced to the KdV equation. Later, in Section 3.2, we will show that internal wave simulations of the full nonlinear and nonhydrostatic equations using the SUNTANS model can be modeled exceptionally well with the much simpler KdV equation. By assuming that the ratio of the layer depths is small, i.e. $h_1/h_2 \ll 1$, we obtain $h_0 \approx h_1$ and $h_1^* = h_1/h_0 \approx 1$. Furthermore, as the lower-layer depth becomes very large the depth-averaged velocity of the lower layer approaches zero. In the limit that $U_2^* \to 0$, the lower-layer momentum Eq. (3) becomes, after integration, to $O(\Delta\rho^*)$:

$$\eta^* = -\xi^* + G(t^*). \tag{8}$$

Here, $G(t^*)$ is an arbitrary function of time, which becomes irrelevant upon insertion of Eq. (8) into Eq. (1). Ignoring the arbitrary function of time, Eq. (8) implies that upon redimensionalization, the amplitude of the free surface is $\Delta\rho^*$ times smaller than the amplitude of the internal interface and of opposite sign.

Substitution of Eq. (8) into the 1-D upper-layer momentum Eq. (1) and recalling that when this relationship is valid, $h_1^* \to 1$, gives:

$$\frac{\partial U^*}{\partial t^*} + \delta U^*\frac{\partial U^*}{\partial x^*} - \frac{\partial \xi^*}{\partial x^*} - \frac{\epsilon^2}{3}\frac{\partial^2}{\partial x^{*2}}\left(\frac{\partial U^*}{\partial t^*}\right) = O(\epsilon^2\delta, \epsilon^4, \Delta\rho^*), \tag{9}$$

$$\frac{\partial \xi^*}{\partial t^*} - \frac{\partial}{\partial x^*}[(1 - \delta\xi^*)U^*] = O(\Delta\rho^*), \tag{10}$$

where it is understood that $U_2^* \to 0$, and hence we refer to the upper-layer velocity as U^*. Eqs. (9) and (10) are sometimes referred to as the reduced gravity model or inverted shallow water equations (as $\epsilon \to 0$) (Cushman-Roisin and Beckers, 2010), because replacing ξ^* with $-\eta^*$ provides the familiar shallow water equations. Eq. (9) is written in the common form of the Boussinesq equations in which the dispersion term appears as two spatial derivatives and one time derivative on the depth-averaged velocity (Grimshaw (2007) following Mei (1983)). However, we can alter the form of these equations while maintaining the same order of accuracy in the asymptotic approximation by self-substitution of the first-order relation of the momentum equation, viz:

$$\frac{\partial U^*}{\partial t^*} = \frac{\partial \xi^*}{\partial x^*} + O(\epsilon^2, \delta, \Delta\rho^*). \tag{11}$$

This was recognized by Peregrine (1967) although the common form (9) was retained. Substitution of the first-order balance (11) into the dispersion term in the momentum Eq. (9) gives, to $O(\epsilon^2\delta, \epsilon^4, \Delta\rho^*)$:

$$\underbrace{\frac{\partial U^*}{\partial t^*}}_{\text{acceleration}} + \underbrace{\delta U^*\frac{\partial U^*}{\partial x^*}}_{\substack{\text{advection of}\\ \text{momentum}}} = \underbrace{\frac{\partial \xi^*}{\partial x^*}}_{\substack{\text{hydrostatic}\\ \text{pressure gradient}}} + \underbrace{\frac{\epsilon^2}{3}\frac{\partial^3 \xi^*}{\partial x^{*3}}}_{\substack{\text{nonhydrostatic}\\ \text{pressure gradient}}}, \tag{12}$$

where the terms are identified to illustrate the related terms in the fully nonhydrostatic and nonlinear equations from which they arise. Recall that the sign of the pressure gradient terms are positive because of the definition of ξ^* from Eq. (8). Eq. (12) is more convenient than (9) because it does not contain mixed time and space derivatives. This will facilitate direct comparison between the physical dispersion arising from the nonhydrostatic pressure and the numerical dispersion arising from discretization errors.

Eqs. (10) and (12) admit bidirectional wave solutions. We restrict our study to unidirectional waves by projecting Eqs. (10) and (12) onto one of their linear characteristics. This gives the KdV equation (derivation of which is given in Zauderer (1989)) governing the evolution of the interface height. The KdV equation, to $O(\epsilon^2\delta, \epsilon^4, \Delta\rho^*)$, is given by

$$\frac{\partial \xi^*}{\partial t^*} + \left(1 - \frac{3}{2}\delta\xi^*\right)\frac{\partial \xi^*}{\partial x^*} + \frac{\epsilon^2}{6}\frac{\partial^3 \xi^*}{\partial x^{*3}} = 0, \tag{13}$$

the solution of which is a wave (train) of depression. Writing the KdV equation (13) in a form similar to the momentum equation (12) gives:

$$\underbrace{\frac{\partial \xi^*}{\partial t^*}}_{\text{acceleration}} - \underbrace{\frac{3}{2}\delta\xi^*\frac{\partial \xi^*}{\partial x^*}}_{\substack{\text{advection of}\\ \text{momentum}}} = -\underbrace{\frac{\partial \xi^*}{\partial x^*}}_{\substack{\text{hydrostatic}\\ \text{pressure gradient}}} - \underbrace{\frac{\epsilon^2}{6}\frac{\partial^3 \xi^*}{\partial x^{*3}}}_{\substack{\text{nonhydrostatic}\\ \text{pressure gradient}}}. \tag{14}$$

The well-known analytical solitary-wave solution to the KdV equation (13) given in Korteweg and de-Vries (1895) is:

$$\xi^* = a^*\,\mathrm{sech}^2\left(\frac{x^* - c^*t^*}{L_0^*}\right), \tag{15}$$

where the wave speed is $c^* = 1 - \delta a^*/2$ and the solitary wave length scale is $L_0^* \equiv \sqrt{-\frac{4}{3}\frac{\epsilon^2}{\delta a^*}}$. Thus the amplitude, a^*, must be negative, hence requiring a wave of depression to ensure real L_0^*.

Although the KdV equation (13) was derived for a two-layer system with a deep lower layer, it can be extended to represent the propagation of weakly nonlinear waves in the presence of arbitrary stratification. Liu et al. (1998) provide an estimation of the nonlinearity, δ, and dispersion, ϵ, parameters for the KdV equation (13) to simulate internal waves in a general two-layer stratified system. These coefficients are given by

$$\delta = \frac{h_2 - h_1}{h_1 h_2}a_0, \tag{16}$$

and

$$\epsilon = \sqrt{\frac{h_1 h_2}{(L_w)^2}}, \tag{17}$$

where a_0 and L_w are the dimensional amplitude and horizontal length scales. Notice that as $h_1 > h_2$, the nonlinear parameter, δ, is negative and thus the internal waves propagate as elevation waves

rather than depression waves. The coefficients in the presence of general stratification are given by

$$\delta = -a_0 \frac{\int_{-d}^{0} \left(\frac{d\phi}{dz}\right)^3 dz}{\int_{-d}^{0} \left(\frac{d\phi}{dz}\right)^2 dz}, \tag{18}$$

and

$$\epsilon = \sqrt{\frac{3}{L_w^2} \frac{\int_{-d}^{0} \phi^2 dz}{\int_{-d}^{0} \left(\frac{d\phi}{dz}\right)^2 dz}}, \tag{19}$$

where $\phi = \phi(z)$ is the first-mode eigenfunction and d is the dimensional depth (Liu, 1988).

2.1. Physical dispersion

In the limit $\delta \to 0$, the momentum (12) and continuity (10) equations are given, to $O(\epsilon^4, \Delta\rho^*)$, by

$$\frac{\partial U^*}{\partial t^*} - \frac{\partial \xi^*}{\partial x^*} - \frac{\epsilon^2}{3} \frac{\partial^3 \xi^*}{\partial x^{*3}} = 0, \tag{20}$$

$$\frac{\partial \xi^*}{\partial t^*} - \frac{\partial U^*}{\partial x^*} = 0. \tag{21}$$

The dispersion relation is obtained via substitution of plane-wave solutions into Eqs. (20) and (21), viz:

$$U^* = \sum \widehat{U}(k) \exp\left(i(kx^* - \omega t^*)\right), \tag{22}$$

$$\xi^* = \sum \hat{\xi}(k) \exp\left(i(kx^* - \omega t^*)\right), \tag{23}$$

where $i = \sqrt{-1}$ is the imaginary unit, k is the nondimensional wavenumber, ω is the nondimensional wave frequency and $\widehat{U}$ and $\hat{\xi}$ are the Fourier amplitudes of each wave component. The resulting dispersion relation is given by

$$\omega^2 = k^2 \left(1 - \frac{1}{3}(k\epsilon)^2\right), \tag{24}$$

or

$$c^2 = \frac{\omega^2}{k^2} = 1 - \frac{1}{3}(k\epsilon)^2, \tag{25}$$

which gives the phase speed $c = \pm\sqrt{1 - \frac{(k\epsilon)^2}{3}}$. Without dispersion, $\epsilon \to 0$, the dispersion relation reduces to that of the nondimensional shallow water equations, $\omega^2 = k^2$, which gives the phase speed $c = \pm 1$. Eqs. (24) and (25) can be compared to the true nondimensional Airy dispersion relation (LeBlond and Mysak, 1978):

$$\omega^2 = \frac{k}{\epsilon}\tanh(k\epsilon) = k^2\left(1 - \frac{1}{3}(k\epsilon)^2 + \frac{2}{15}(k\epsilon)^4 - \frac{17}{315}(k\epsilon)^6 + \cdots\right), \tag{26}$$

with

$$c^2 = \frac{\omega^2}{k^2} = \frac{1}{k\epsilon}\tanh(k\epsilon) = 1 - \frac{1}{3}(k\epsilon)^2 + \frac{2}{15}(k\epsilon)^4 - \frac{17}{315}(k\epsilon)^6 + \cdots. \tag{27}$$

These show that the Boussinesq equations recover the Airy dispersion relation to $O((k\epsilon)^4)$. The third-order derivative term in the momentum equation (12) appearing from the first-order nonhydrostatic effect, $\frac{\partial^3 \xi^*}{\partial x^{*3}}$, called the dispersion term, is aptly named because it is responsible for deviation from shallow-water behavior. Furthermore, the coefficient in front of this term is the lowest-order physical dispersion coefficient.

The dispersion relation for the KdV equation is similar to that for the Boussinesq equations. The linear KdV equation ($\delta \to 0$) is given by

$$\frac{\partial \xi^*}{\partial t^*} + \frac{\partial \xi^*}{\partial x^*} + \frac{\epsilon^2}{6} \frac{\partial^3 \xi^*}{\partial x^{*3}} = 0. \tag{28}$$

Substitution of the plane-wave solution into Eq. (28) gives:

$$\omega = k\left(1 - \frac{(k\epsilon)^2}{6}\right), \tag{29}$$

or

$$c = \frac{\omega}{k} = 1 - \frac{(k\epsilon)^2}{6}. \tag{30}$$

The dispersion relation (29) differs from the Boussinesq dispersion relation (24) by a quadratic factor arising from the assumption of unidirectional waves in the KdV equation. The dispersion relations (24) and (29) show that the physically-dispersive properties are controlled by the parameter $k\epsilon$ which represents the degree of nonhydrostasy or ratio of the depth to the horizontal wavelength.

2.2. Numerical dispersion

For illustrative purposes we will discretize the KdV equation (13) using centered finite-differences in both space and time. Central differencing in time is known as "leap-frog", and is used in several ocean models (POM, Blumberg and Mellor, 1987; MICOM, Bleck et al., 1992; MOM, Pacanowski and Griffes, 1999). Many ocean models use second-order accurate central differencing for the baroclinic pressure gradient term (Shchepetkin and McWilliams, 2003). As we will show, the discretization of this term is primarily responsible for numerical dispersion. The discretization of the nonlinear advection of momentum, although often believed to dominate the effects of numerical dispersion (Hodges et al., 2006; Scotti and Mitran, 2008), has a much weaker effect, since typically $\delta < O(1)$.

The second-order accurate in time and space discretization of the KdV equation (13) is given by

$$\frac{\xi_i^{n+1} - \xi_i^{n-1}}{2\Delta t^*} + \left(1 - \frac{3}{2}\delta\xi_i^n\right)\frac{\xi_{i+1}^n - \xi_{i-1}^n}{2\Delta x^*} + \frac{\epsilon^2}{6}\frac{\frac{1}{2}\xi_{i+2}^n - \xi_{i+1}^n + \xi_{i-1}^n - \frac{1}{2}\xi_{i-2}^n}{\Delta x^{*3}} = 0, \tag{31}$$

where the superscript n represents the time index and the subscript i represents the spatial index or individual grid point of the numerical solution on a discrete grid, i.e. $\xi_i^n = \xi^*(x_i^*, t_n^*) = \xi^*(i\Delta x^*, n\Delta t^*)$. The second-order accurate spatial discretization of the dispersion term in Eq. (31) ensures that truncation errors are $O(\epsilon^2(\Delta x^*)^2)$ and thus numerical error associated with this term is much smaller than the retained terms.

The modified equivalent partial differential form of the spatial gradient term in Eq. (31), as obtained by expansion of the numerical solution in a Taylor series, is given by

$$\frac{\xi_{i+1}^n - \xi_{i-1}^n}{2\Delta x^*} = \left.\frac{\partial \xi^*}{\partial x^*}\right|_i^n + \left.\frac{\Delta x^{*2}}{6}\frac{\partial^3 \xi^*}{\partial x^{*3}}\right|_i^n + \left.\frac{\Delta x^{*4}}{120}\frac{\partial^5 \xi^*}{\partial x^{*5}}\right|_i^n + \left.\frac{\Delta x^{*6}}{5040}\frac{\partial^7 \xi^*}{\partial x^{*7}}\right|_i^n + O\left(\Delta x^{*8}\right). \tag{32}$$

Therefore, to $O(\Delta x^{*2})$, the second-order accurate, central finite-difference approximation is consistent with the first derivative at the grid point i and time-level n. To derive the modified equivalent partial differential equation (MEPDE) of the KdV equation (13) we use expansions similar to Eq. (32) for all finite-difference terms in

Eq. (31). Furthermore, the linear Eq. (28) can be used to convert the higher-order time derivatives to spatial derivatives. To $O(\epsilon^2,\delta)$, Eq. (28) gives:

$$\frac{\partial^m \xi^*}{\partial t^{*m}} = (-1)^m \frac{\partial^m \xi^*}{\partial x^{*m}}, \tag{33}$$

where m is the order of the partial derivative. Thus the MEPDE of the discrete KdV equation (31) after removing subscript i and superscript n (since the equation holds for all discrete space and time), is given by

$$\frac{\partial \xi^*}{\partial t^*} + \left(1 - \frac{3}{2}\delta\xi^*\right)\frac{\partial \xi^*}{\partial x^*} + \left(\frac{\epsilon^2}{6} + \beta\right)\frac{\partial^3 \xi^*}{\partial x^{*3}} = O\left(\epsilon^2\Delta x^{*2}, \delta\Delta x^{*2}, \Delta x^{*4}, \Delta t^{*4}\right), \tag{34}$$

where $\beta = (1 - C^2)\frac{\Delta x^{*2}}{6}$ and $C \equiv \frac{\Delta t^*}{\Delta x^*}$ is the Courant number (see Appendix A for derivation). This shows that the modified form of the KdV equation resulting from second-order accurate, central finite-difference approximation in time and space differs from the original KdV equation (13) due to the addition of numerical dispersion of magnitude β. Here, β is the lowest-order numerical dispersion coefficient arising from the discretization of the linear pressure gradient term. Note that a Courant number satisfying $C^2 > 1 + (\epsilon/\Delta x^*)^2$ may lead to *negative* dispersion and instability.

2.3. Comparison of numerical and physical dispersion

We can rewrite Eq. (34) after factoring the physical dispersion coefficient, $\epsilon^2/6$, as:

$$\frac{\partial \xi^*}{\partial t^*} + \left(1 - \frac{3}{2}\delta\xi^*\right)\frac{\partial \xi^*}{\partial x^*} + (1 + \Gamma)\frac{\epsilon^2}{6}\frac{\partial^3 \xi^*}{\partial x^{*3}} = O\left(\epsilon^2\Delta x^{*2}, \delta\Delta x^{*2}, \Delta x^{*4}, \Delta t^{*4}\right), \tag{35}$$

where Γ, the ratio of numerical to physical dispersion, is given by

$$\Gamma = \frac{\beta}{\frac{\epsilon^2}{6}} = \frac{(1 - C^2)\frac{\Delta x^{*2}}{6}}{\frac{\epsilon^2}{6}} = (1 - C^2)\frac{\Delta x^{*2}}{\epsilon^2} = K\left(\frac{\Delta x^*}{\epsilon}\right)^2, \tag{36}$$

with $K = 1 - C^2$. We write Eq. (35) in this form to show that numerical discretization of the governing equation increases the magnitude of dispersion by a factor of $1 + \Gamma$, due to the presence of numerical dispersion. The modified dispersion relation of the linearized version of Eq. (35), to $O((k\epsilon)^4, (k\Delta x^*)^4)$, is given by

$$\omega = k\left(1 - (1 + \Gamma)\frac{(k\epsilon)^2}{6}\right), \tag{37}$$

which gives:

$$c = 1 - (1 + \Gamma)\frac{(k\epsilon)^2}{6}. \tag{38}$$

Eq. (38) shows that both physical and numerical dispersion (assuming $C^2 \leqslant 1 + (\epsilon/\Delta x^*)^2$) reduce the speed of the waves. Comparing Eqs. (35) and (37) to (29) and (30), respectively, shows that the numerical solution will be consistent with the true solution when Γ is small, meaning that the numerical effects of dispersion are small in comparison to the physical effects. When $\Gamma \geqslant O(1)$, the phase speed of short waves ($k\epsilon \geqslant O(0.1)$) may be significantly affected by the additional (artificial) dispersion. The ratio Γ, as seen in Eq. (36), becomes zero when the Courant number is 1, and all error in the MEPDE is eliminated. This is an ideal case and in general, the Courant number will not be 1. However, a Courant number near 1 for this discretization decreases the magnitude of Γ since as $C \to 1, K \to 0$. For moderate and low Courant numbers the coefficient K has little effect on the order of magnitude of Γ.

It is important to note that the constant K in Eq. (36) is determined by both the spatial and temporal discretization of the equations. The primary source of numerical dispersion for the KdV equation (13), based on the central discretization (31), is the spatial discretization of the horizontal pressure gradient. The spatial discretization of this term in Eq. (31) provides the 1 in the constant K, while the time-discretization reduces K by C^2. If the time discretization were carried out to 3rd-order or greater, while using second-order central differences on the linear gradient term, then the constant would be $K = 1$. If instead of leap-frog we employ the semi-implicit θ-method (Casulli and Cattani, 1994) for the temporal discretization of the KdV equation (13), we obtain the same MEPDE as Eq. (35), but with $K = 1 + \frac{C^2}{2}$. Therefore, for most popular second-order accurate methods (in either space or time) the ratio of numerical to physical dispersion should be of the form $\Gamma = K(\Delta x^*/\epsilon)^2$, where for most practical implementations K is an $O(1)$ constant.

In terms of dimensional parameters, the ratio of numerical to physical dispersion is given by

$$\Gamma = K\left(\frac{\Delta x^*}{\epsilon}\right)^2 = \frac{\left(\frac{\Delta x}{L_w}\right)^2}{\left(\frac{h_1}{L_w}\right)^2} = K\left(\frac{\Delta x}{h_1}\right)^2 = K\lambda^2, \tag{39}$$

where $\lambda \equiv \Delta x/h_1$ is the grid leptic ratio (Scotti and Mitran, 2008), or lepticity. To ensure relative dominance of physical over numerical effects, simulations require $\Gamma \ll 1$. Since the ratio of numerical to physical dispersion is given by $\Gamma = K\lambda^2$, the condition $\Gamma \ll 1$ is met when $\lambda < O(1)$ or $\Delta x < h_1$.

If instead we redimensionalize the nonhydrostatic parameter appearing in the KdV equation with the general two-layer expression given in Eq. (17), then the form of Γ for a general two-layer system is given by

$$\Gamma = K\left(\frac{\Delta x^*}{\epsilon}\right)^2 = K\frac{\left(\frac{\Delta x}{L_w}\right)^2}{\left(\sqrt{\frac{h_1 h_2}{(L_w)^2}}\right)^2} = K\frac{\left(\frac{\Delta x}{L_w}\right)^2}{\frac{h_1 h_2}{(L_w)^2}} = K\frac{\Delta x^2}{h_1 h_2} = K\lambda_1\lambda_2, \tag{40}$$

where $\lambda_1 \equiv \Delta x/h_1$ and $\lambda_2 \equiv \Delta x/h_2$. In this case, the requirement that $\Gamma \ll 1$ is met when $\lambda_1\lambda_2 \ll 1$. Equivalently, this condition is met when both $\lambda_1 < O(1)$ and $\lambda_2 < O(1)$, or when $\Delta x < \min(h_1, h_2)$. For a general stratification, Eq. (19) can be used to show that:

$$\Gamma = K\left(\frac{\Delta x^*}{\epsilon}\right)^2 = K\frac{\left(\frac{\Delta x}{L_w}\right)^2}{\left(\sqrt{\frac{3}{(L_w)^2}\frac{\int_{-d}^{0}\phi^2 dz}{\int_{-d}^{0}\left(\frac{\partial\phi}{\partial z}\right)^2 dz}}\right)^2} = K\frac{\Delta x^2}{h_e^2} = K\lambda_e^2, \tag{41}$$

where $\lambda_e \equiv \Delta x/h_e$, and the equivalent depth in a continuously-stratified fluid of depth d is given by

$$h_e = \sqrt{\frac{3\int_{-d}^{0}\phi^2 dz}{\int_{-d}^{0}\left(\frac{\partial\phi}{\partial z}\right)^2 dz}}.$$

For a linearly-stratified fluid, $\phi = \sin(\pi z/d)$, which gives $h_e = \frac{\sqrt{3}}{\pi}d \approx 0.55d$. In the presence of linear stratification, the horizontal grid resolution must therefore be less than roughly one-half the water depth in order for the numerical dispersion to be less than the physical dispersion.

The MEPDE analysis has identified the dominant numerical dispersion term for second-order accurate methods that is proportional to $(k\Delta x^*)^2$. The parameter $k\Delta x^*$ can be interpreted as the degree to which the variability of a wave is resolved on a discrete grid. Slowly-varying waves on fine grids result in small values of $k\Delta x^*$ and little numerical error. On the other hand, short waves on coarse grids give large values of $k\Delta x^*$ and result in significant error.

2.4. Modeled solitary wave widths

The presence of numerical dispersion affects the width of modeled solitary-like waves. The analytical soliton length scale derived from the analytical solution to the KdV equation (13) is given by

$$L_0^* \equiv \sqrt{-\frac{4}{3}\frac{\epsilon^2}{\delta a^*}}. \tag{42}$$

Modeled soliton length scales can be derived from the analytical solution to the modified equivalent KdV equation (34), which is similar to analytical solution of the KdV equation (15) and is given by

$$\xi^* = a^* \operatorname{sech}^2\left(\frac{x^* - c^* t^*}{L^*}\right), \tag{43}$$

where the modeled soliton length scale is:

$$L^* = \sqrt{-8\frac{\epsilon^2/6+\beta}{\delta a^*}} = \sqrt{-\frac{4}{3}\frac{(1+\Gamma)\epsilon^2}{\delta a^*}} = \sqrt{1+\Gamma}\sqrt{-\frac{4}{3}\frac{\epsilon^2}{\delta a^*}} = L_0^*\sqrt{1+\Gamma}. \tag{44}$$

In hydrostatic simulations, the artificial soliton length scale is given by

$$L_h^* = \sqrt{-8\frac{\beta}{\delta a^*}} = \sqrt{-8\frac{\Gamma\epsilon^2/6}{\delta a^*}} = \sqrt{\Gamma}\sqrt{-\frac{4}{3}\frac{\epsilon^2}{\delta a^*}} = L_0^*\sqrt{\Gamma}, \tag{45}$$

which primarily depends on the form of the numerical dispersion coefficient, β, and thereby depends on the grid resolution (recall $\beta \sim (\Delta x^*)^2$). We note that the soliton length scales given above are approximately half of the half-width, or more precisely half of the $\operatorname{sech}^2(1) \approx 42\%$-width. Based on the scaling of L_h^*, we can determine a relationship between the grid spacing and the length scale of the artificial soliton, which is given by

$$\frac{\Delta x^*}{L_h^*} = \frac{\Delta x^*}{\sqrt{-8\frac{\beta}{\delta a^*}}} \sim \frac{\Delta x^*}{\sqrt{\frac{(\Delta x^*)^2}{\delta}}} = \frac{\Delta x^*}{\Delta x^*\sqrt{\frac{1}{\delta}}} = \sqrt{\delta}. \tag{46}$$

Therefore, as the nonlinearity increases, the widths of numerical solitons approach the grid scale. We can determine a similar relationship between the grid spacing and the length scale of the analytical solitons, which is given by

$$\frac{\Delta x^*}{L_0^*} = \frac{\Delta x^*}{\sqrt{-\frac{4}{3}\frac{\epsilon^2}{\delta a^*}}} = \Delta x^*\sqrt{-\frac{3}{4}\frac{\delta a^*}{\epsilon^2}} = \frac{\Delta x^*}{\epsilon}\sqrt{-\frac{3}{4}\delta a^*} \sim \frac{\Delta x^*}{\epsilon} = \lambda. \tag{47}$$

This equation provides an alternative interpretation of the parameter λ. When λ is large, the grid does not resolve the analytical soliton length scale, and error ensues.

Assuming that the ratio of numerical to physical dispersion scales like the grid lepticity squared, viz. $\Gamma = K\lambda^2$, we can investigate how soliton widths scale with the grid lepticity. Substituting $\Gamma = K\lambda^2$ into Eq. (44), we obtain:

$$L^*/L_0^* = L/L_0 = \sqrt{1+K\lambda^2}. \tag{48}$$

Substituting $\Gamma = K\lambda^2$ into Eq. (45), we obtain:

$$L_h^*/L_0^* = L_h/L_0 = \lambda\sqrt{K}. \tag{49}$$

Therefore, for hydrostatic models, the numerical soliton widths scale linearly with the grid lepticity. We note that since the nondimensional variables are all normalized by the same length scale, Eqs. (48) and (49) hold for dimensional models. In the following numerical experiments, we compare modeled (dimensional) soliton widths to the theoretical soliton length scales derived above, i.e. L_0, L, L_h.

3. Numerical experiments

3.1. Assessing numerical dispersion in the discrete KdV equation

We present numerical simulations of the KdV equation to illustrate some similarities and differences between hydrostatic and nonhydrostatic behavior. In what follows, we refer to the standard KdV equation (13) as the "nonhydrostatic equation", and refer to the KdV equation without dispersion ($\epsilon = 0$) as the "hydrostatic equation". We will show that the results of the two models can be almost identical when the numerical dispersion, present in both models, is much larger than the physical dispersion in the nonhydrostatic model, and hence dominates the solution of both equations.

The numerical experiments are performed with the second-order accurate discretization of the KdV equation given in Eq. (31). A grid-refinement convergence analysis verifying that the method is indeed second-order accurate is given in Appendix B. The following simulations use the parameters $\epsilon = 0.1$ and $\delta = 0.2$, which are chosen to approximately match the internal wave scales given in Apel et al. (1985). An Asselin filter (Asselin, 1972), popular with several ocean models using the leap-frog time discretization, with the nominal coefficient of 0.05 is also employed. The Asselin filter prevents the onset of high wavenumber error. For simulations of short duration, the model results (not shown) are identical with and without the filter. The simulations are performed in a periodic domain of length $L_d^* = 10$, and the number of equispaced grid points that are used to discretize the domain is varied to study the effects of Γ. The initial condition is given by

$$\xi^*(x^*, t^* = 0) = \exp\left[-\left(\frac{x^* - 2}{\sigma^*}\right)^2\right], \tag{50}$$

where $\sigma^* = 0.85$. The Courant number is given by $C = \frac{\Delta t^*}{\Delta x^*} = 0.01$.

Fig. 2 shows the result when $N_x = 1000$ grid points are used which gives $\Gamma = 0.01$. Both the hydrostatic (solid, red line) and nonhydrostatic (dashed, blue line) results lead to trains of solitary waves that emerge from the initial Gaussian of depression. However, since the numerical dispersion is 100 times smaller that the physical dispersion, the nonhydrostatic simulation is very close to the exact solution. Having considerably less dispersion (all of which is numerical), the hydrostatic simulation forms a number of sharp and narrow numerically-induced solitons. These arise from the balance between nonlinearity and weak (numerical) dispersion.

Fig. 2 also shows the leading solitons from the hydrostatic and nonhydrostatic simulations compared to the analytical solitons. The analytical solitons are given by $\xi^* = a^* \operatorname{sech}^2\left((x^* - x_0^*)/L_{th}^*\right)$, where a^* is the amplitude of the leading soliton centered at $x^* = x_0^*$. For the nonhydrostatic result, $L_{th}^* = L_0^*$ from Eq. (42) (since $\Gamma \ll 1$), while for the hydrostatic result $L_{th}^* = L_h^*$ from Eq. (45). In addition to the specified values of δ and ϵ, L_0^* and L_h^* require computation of a^* and x_0^*. These are obtained with a quadratic polynomial fit to the three points nearest the maximum value (in absolute value) of the interface deflection ξ^*. The amplitude a^* is given by the maximum of this polynomial and x_0^* is the location of this maximum. The figure shows that the theoretical solitons with scales L_0^* and L_h^* both agree with the simulation results for the nonhydrostatic and hydrostatic simulations, respectively. Also noteworthy in Fig. 2 is the weak dependence of L_0^* and L_h^* on the wave amplitude as demonstrated by the similar widths of the individual solitons in the wave packets.

Fig. 3 shows the same calculation as in Fig. 2 but with $N_x = 32$ grid points and $\Gamma = 10$. In this simulation, the dispersive characteristics are primarily numerically-induced and thus the results of the hydrostatic and nonhydrostatic simulations are virtually identical. Furthermore, the length scale of the solitary waves, $L^* \approx 0.25\sqrt{1+\Gamma} \approx 0.85$, is approximately the same as the length scale of the initial Gaussian function and thus the initial wave form propagates as a (single) solitary wave.

Fig. 3 also compares the leading solitons to the analytical solitons. The numerical soliton of width L_h^* compares very well with the results from both the hydrostatic and nonhydrostatic models.

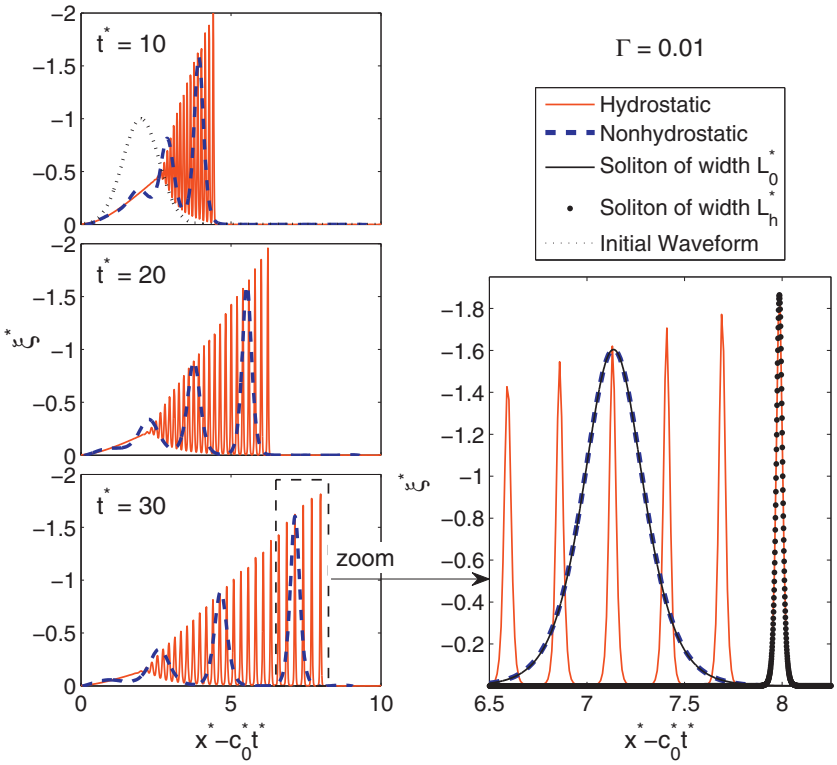

Fig. 2. The results of a nonhydrostatic simulation (dashed blue line) vs. a hydrostatic simulation (solid red line) for the case when $\Gamma = 0.01$. The plot in the lower-right depicts a zoomed-in view of the simulation along with a comparison between the theoretical sech^2 profiles and the numerical results. Recall that the nondimensional linear wave speed is $c_0^* = 1$. (For interpretation of the references to colour in this figure legend, the reader is referred to the web version of this article.)

These solitons are approximately three times larger than the analytical soliton of width L_0^*. The length scales of the solitons are a good indicator of the form of dispersion, and thus we can see that in this simulation the magnitudes of dispersion in each model are roughly equivalent.

3.2. Assessing numerical dispersion in the nonhydrostatic SUNTANS model

We simulate the evolution of an internal solitary-like wave train using the nonhydrostatic SUNTANS model (Fringer et al., 2006) in a two-dimensional x-z domain. The parameters are chosen to approximately mimic the evolution of solitary-like waves in the South China Sea, which evolve from internal tides generated at the Luzon Strait at its eastern boundary (Zhang et al., 2011). Simulations are performed on a domain of length $L_d = 300$ km and depth $d = 2000$ m that is initialized with approximate two-layer stratification as an idealized representation of the South China Sea so as to simplify our analysis. Despite the idealized stratification, the simulated solitary-like waves are similar to those that form in the South China Sea, particularly from the point of view of relevant length scales.

The initial stratification is given by

$$\frac{\rho(x,z,t=0)}{\rho_0} = -\frac{1}{2}\frac{\Delta\rho}{\rho_0}\tanh\left[\frac{2\tanh^{-1}\alpha}{d_\rho}(z-\xi(x,t=0)+h_1)\right], \tag{51}$$

where the upper-layer depth is $h_1 = 250$ m, the $\alpha = 99\%$ interface thickness (see Fringer and Street (2003)) is $d_\rho = 200$ m, and the density difference is given by $\Delta\rho/\rho_0 = 0.001$. The initial Gaussian of depression that evolves into a train of solitary-like waves is given by

$$\xi(x,t=0) = -G_0\exp\left[-\left(\frac{x}{w_\rho}\right)^2\right], \tag{52}$$

with $G_0 = 250$ m and $w_\rho = 15$ km. The boundary conditions are closed at $x = 0$ and $x = L_d$ and the bottom at $z = -d$ is free-slip with a free surface at the upper boundary. The domain is discretized uniformly in the vertical with $N_z = 100$ grid cells, and we perform six simulations each with a different uniform horizontal resolution containing $N_x = 150$, 300, 600, 1200, 2400, and 4800 cells, such that the grid lepticity $\lambda = \Delta x/h_1$ varies from 0.25 to 8, and where $\Delta x = L_d/N_x$. We did not change the vertical resolution because this has little influence on the results as long as the stratification is reasonably resolved. The time step is determined with the horizontal Courant number which is held fixed for all simulations, and is given by $C_h = c_0\Delta t/\Delta x = 0.11$, where $c_0 = 1.4$ m s^{-1} is the first-mode eigenspeed obtained from a linearized modal analysis. The simulations are run for a total time of 145,600 s (roughly 1.7 days), so that the finest grid requires $\Delta t = 5$ s for a total of 29,120 time steps. Although rotational effects lead to added linear dispersion which has a tendency to broaden waves that propagate over inertial time scales (Helfrich and Melville, 2006), rotation is ignored in the present simulations. To stabilize the central-differencing scheme for momentum advection, the horizontal and vertical eddy-diffusivities are constant and are given by $\nu_H = 0.1$ m^2 s^{-1} and $\nu_V = 10^{-4}$ m^2 s^{-1}, respectively, and no scalar diffusivity is employed.

In what follows we compare the results of the hydrostatic to the nonhydrostatic versions of SUNTANS. Since the nonhydrostatic code essentially computes a correction to the hydrostatic dynamics, switching between the two codes is straightforward although the nonhydrostatic code incurs more overhead particularly for low values of the grid lepticity. Fig. 4 shows the computational overhead associated with using the nonhydrostatic model as measured by the ratio of the total wallclock simulation time for the

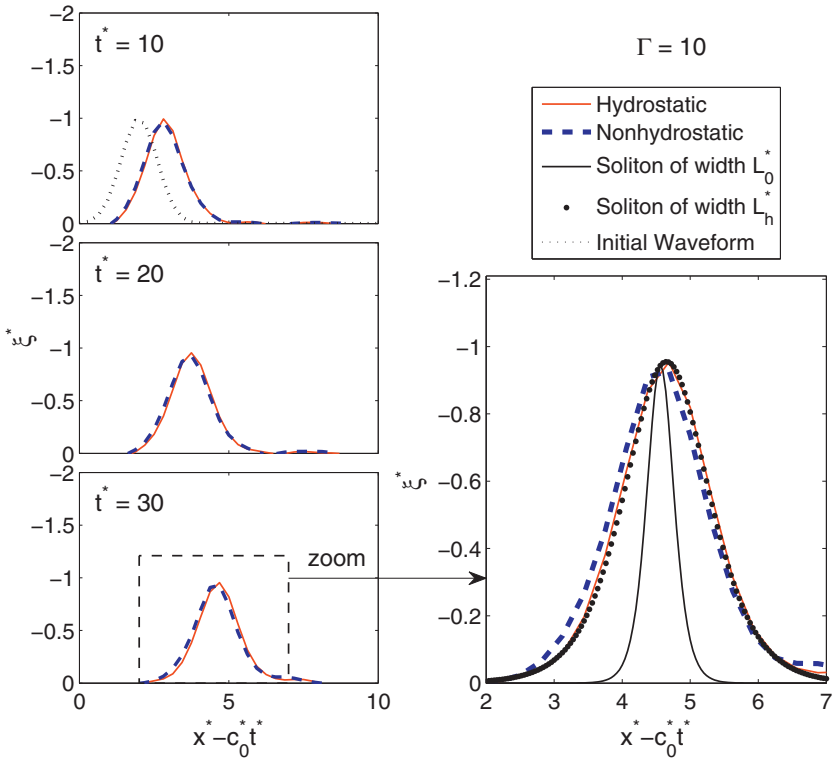

Fig. 3. The results of a nonhydrostatic simulation (dashed blue line) vs. a hydrostatic simulation (solid red line) for the case when $\Gamma = 10$. The plot in the lower-right depicts a zoomed-in view of the simulation along with a comparison between the theoretical sech^2 profiles and the numerical results. Recall that the nondimensional linear wave speed is $c_0^* = 1$. (For interpretation of the references to colour in this figure legend, the reader is referred to the web version of this article.)

nonhydrostatic model to that for the hydrostatic model. For large grid lepticity there is relatively little overhead because the preconditioner for the nonhydrostatic pressure solver performs well when the grid aspect ratio $\Delta z/\Delta x$ is small (Fringer et al., 2006). However, the preconditioner is not as effective for larger grid aspect ratios, or equivalently smaller grid leptic ratios. Therefore, for the smallest lepticity the nonhydrostatic code requires roughly 8 times as much wallclock time than the hydrostatic simulation (the most well-resolved nonhydrostatic run took 2 s per time step using 16 cores on four quad-core Opteron 2356 QC processors). It is interesting to note that the nonhydrostatic overhead diverges sharply around $\lambda = 2$, which is effectively the limit above which physical nonhydrostatic effects are overwhelmed by numerical nonhydrostatic effects. Marshall et al. (1997) show that, due to the performance of the preconditioner, nonhydrostatic algorithms in the hydrostatic limit are no more computationally expensive than hydrostatic models. They describe the nonhydrostatic pressure solver and preconditioner as "an algorithm that seamlessly moves from nonhydrostatic to hydrostatic limits". We note, however, that a nonhydrostatic model does not behave correctly until it resolves the magnitude of dispersion, that is, $\lambda < O(1)$. Furthermore, as shown in Fig. 4, truly resolving nonhydrostatic effects is more computationally expensive.

To infer the behavior of the numerical dispersion in the SUNTANS simulations, we first show that the SUNTANS results are accurately represented by the KdV equation. We compare the results of the highest resolution SUNTANS model ($N_x = 4800$) with the KdV model with $N_x = 800$, so that $\Gamma \approx 0.25$ in both models. The nondimensional initial condition for the SUNTANS model is given by

$$\xi_S^*(x^*, t^* = 0) = -a_S^* \exp\left[-\left(\frac{x^*}{\sigma_S^*}\right)^2\right], \tag{53}$$

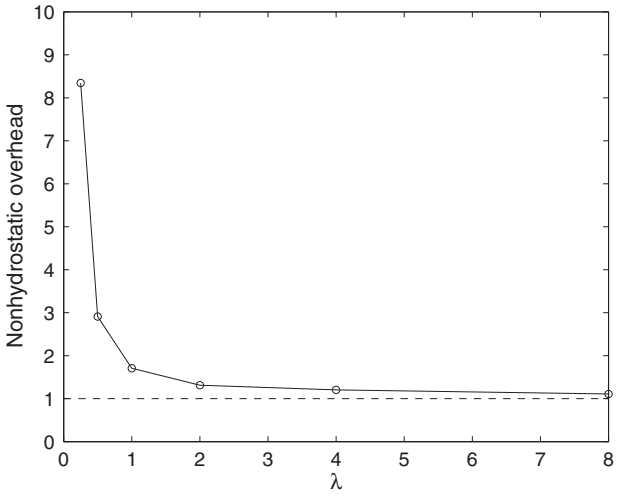

Fig. 4. Relative workload associated with computing the nonhydrostatic pressure as a function of the grid lepticity $\lambda = \Delta x/h_1$. The overhead is computed as the ratio of the total wallclock time for the nonhydrostatic simulation to that of the hydrostatic simulation.

where $a_S^* = G_0/a_0 = 1.136$ and $\sigma_S^* = w_\rho/L_w = 10.446$. In this example, the results from the SUNTANS model are nondimensionalized with $a_0 = 220$ m and $L_w = L_0 = 1436$ m, which are the amplitude and length scale, respectively, of the leading solitary wave at the end of the highest resolution simulation. If we approximate the SUNTANS initial condition as a two-layer stratification, Eqs. (16) and (17) give the KdV parameters $\delta = 0.754$ and $\epsilon = 0.461$. The continuous stratification parameter estimates from Eqs. (18) and (19) give similar values of $\delta = 0.756$ and $\epsilon = 0.494$. Because the KdV

equation only admits right-propagating waves, the initial condition for the KdV model needs to be adjusted to produce the same waves as the SUNTANS model. The SUNTANS model produces right-propagating waves because its initial condition is given by a half-Gaussian of depression at the left no-flux boundary. The initial condition for the KdV model is therefore given by

$$\xi_K^*(x^*, t^* = 0) = -a_K^* \exp\left[-\left(\frac{x^* - \Delta x_K^*}{\sigma_K^*}\right)^2\right], \tag{54}$$

where $a_K^* = 0.536, \sigma_K^* = \sigma_S^* = 10.446$, and $\Delta x_K^* = 1.253$. Due to the different initial conditions, the parameters required to produce a match between the KdV result and the SUNTANS model are given by $\delta = 0.572$ and $\epsilon = 0.585$. As shown in Fig. 5, the agreement between the KdV equation and the SUNTANS model is excellent. The only significant deviation between the two models arises from the tail of the wave train which is produced by numerical diffusion in the SUNTANS model that is not present in the KdV model. The slight mismatch between the theoretical parameters, δ and ϵ, given by Eqs. (16)–(19) and the best fit parameters is due to higher-order nonlinearity and the finite-thickness of the interface, which are not accounted for in the KdV theory.

The excellent agreement between the models highlights the power of the relatively simple KdV equation for modeling complex phenomena. Of course, there are many situations in which the KdV equation does not adequately capture the dynamics of the fully nonlinear and nonhydrostatic model for a continuously stratified system. However, this result shows that the dominant physics of internal waves at the limits of weakly nonlinear, weakly nonhydrostatic characterization can still be represented by the KdV equation. We make this comparison to argue that the analysis performed for the KdV equation with regard to numerical vs. physical dispersion should hold for fully nonhydrostatic models for certain problems of interest. That is, for weakly nonlinear, weakly nonhydrostatic internal wave phenomena even in a continuously stratified system modeled with a (second-order accurate) nonhydrostatic model, the ratio of numerical to physical dispersion

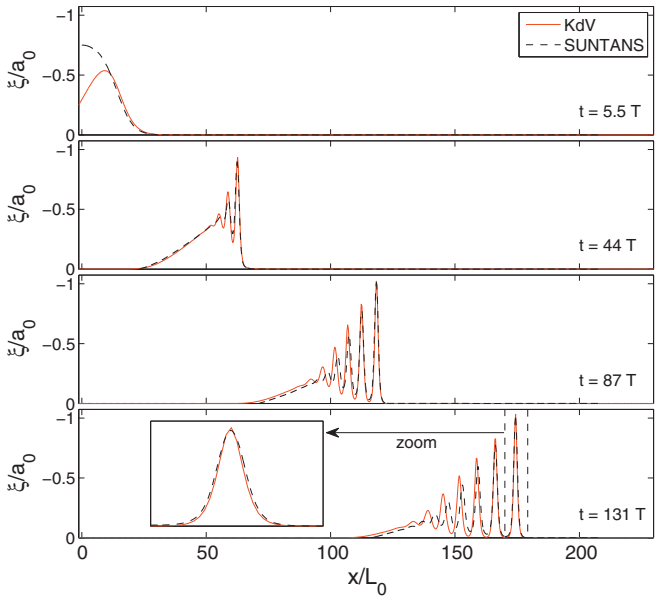

Fig. 5. Comparison of the KdV equation to the nonhydrostatic SUNTANS ocean model. The KdV solution is for the interface height in a two-layer system. SUNTANS models a continuously stratified system in which the $\rho = \rho_0$ density contour represents the solution. The cutout in the bottom subplot shows a comparison of the leading soliton.

should be $\Gamma = K\lambda^2$ as is the case for the KdV equation. With this in mind, we compare the results of hydrostatic and nonhydrostatic simulations using SUNTANS at various resolutions as we did for the KdV equation in Figs. 2 and 3.

Fig. 6 shows the nonhydrostatic SUNTANS result compared to the hydrostatic result for the finest grid ($N_x = 4800$), or the smallest leptic ratio $\lambda = \Delta x/h_1 = 0.25$. In the figure, time is normalized by $T_s = L_w/c_0$, where $L_w = L_0 = 1436$ m is the leading solitary wave width at the end of the simulation. As expected, the nonhydrostatic result leads to a train of rank-ordered solitary-like internal gravity waves of depression that move faster than the linear phase speed (as indicated by the vertical dashed lines in Fig. 6). Owing to amplitude dispersion, the hydrostatic wave train also propagates faster than the linear phase speed c_0. However, due to a lack of physical dispersion, the wave steepens into a train of very short solitary-like waves (see the inset plot at $t = 141.5\ T_s$). These short waves represent a balance between nonlinear steepening and numerical dispersion that results from the second-order error in the discretization of the baroclinic pressure gradient in SUNTANS. Due to the high grid resolution, the relatively small lepticity of $\lambda = \Delta x/h_1 = 0.25$ is the cause of the weak numerical dispersion. Unlike the results from the KdV simulations in Section 3.1, the SUNTANS results also possess numerical diffusion. Therefore, the nearly grid-scale length of the numerically-induced solitary-like waves results in numerical diffusion that leads to amplitude loss in the leading solitary-like waves as well as a thickening of the stratification in the lee of the wave train. The amplitude loss leads to weaker amplitude dispersion for the hydrostatic case and causes the hydrostatic packet to propagate more slowly than the nonhydrostatic packet. The problem of excess numerical diffusion associated with high-resolution hydrostatic models was recognized by Hodges et al. (2006), who hypothesized that formation of numerical "soliton-like" waves leads to numerical diffusion and dissipation. Our results support this hypothesis. However, we add that the lack of dispersion (physical or otherwise) in high-resolution hydrostatic models is the cause of problems with numerical diffusion and dissipation.

When the lepticity is increased to $\lambda = 8$, numerical dispersion is so large relative to physical dispersion that the nonhydrostatic and hydrostatic results are nearly identical, as shown in Fig. 7. This result agrees with Marshall et al. (1997) who conclude that at coarse horizontal resolution, hydrostatic and nonhydrostatic models give essentially the same numerical solutions. Although the results look qualitatively similar, the nonhydrostatic result is far too dispersive due to the numerical dispersion, and so the width of the leading wave is larger than the "exact" result shown in Fig. 6.

As shown in Fig. 8, increasing the grid lepticity causes the width of the leading solitary-like waves to grow in both the hydrostatic and nonhydrostatic solutions. The width of the nonhydrostatic wave, however, converges to the correct value upon decreasing the lepticity, while that for the hydrostatic waves continues to decrease toward zero. This decrease leads to more numerical diffusion which causes the hydrostatic wave to propagate more slowly. These results indicate that the width of the leading solitary-like wave in the wave packets is a good indicator of the numerical dispersion. Since the dispersion in the hydrostatic model is strictly numerical, then progressively weaker dispersion with grid refinement leads to shorter solitary-like waves, while the waves in the nonhydrostatic model converge to the correct solution with grid refinement. Increased grid spacing leads to larger solitary-wave widths in both models, although the width of the waves in the nonhydrostatic model will always be larger than those in the hydrostatic model due to the presence of physical dispersion. While always present, the relative magnitude of the resolved physical dispersion decreases with increasing grid lepticity.

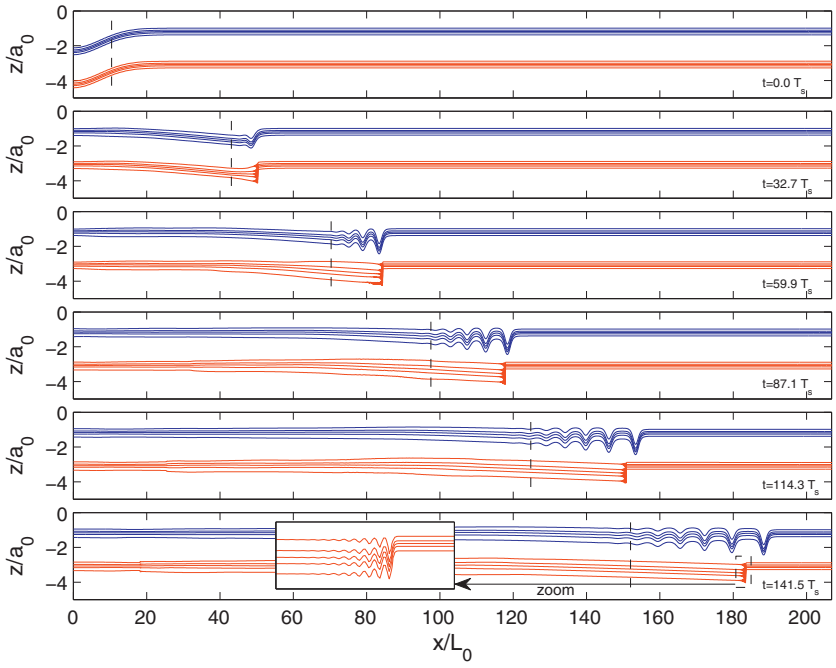

Fig. 6. Comparison of the evolution of a solitary-like internal gravity wave train as computed by SUNTANS with $N_x \times N_z = 4800 \times 100$ grid cells ($\lambda = \Delta x/h_1 = 0.25$) with (upper blue contours) and without (lower red contours) the nonhydrostatic pressure. The horizontal distance is normalized by $L_w = L_0 = 1436$ m, the width of the leading nonhydrostatic wave at the end of the simulation, and $T_s = L_w/c_0$ is the wave propagation time scale. Density contours are shown for $\rho/\rho_0 = (-0.4, -0.2, 0, 0.2, 0.4)\Delta\rho/\rho_0$. A zoomed-in view of the dashed box around the leading wave in the hydrostatic wave train is depicted in the inset plot at $t = 141.5\ T_s$. The vertical dashed line moves at the linear wave speed c_0 for reference. (For interpretation of the references to colour in this figure legend, the reader is referred to the web version of this article.)

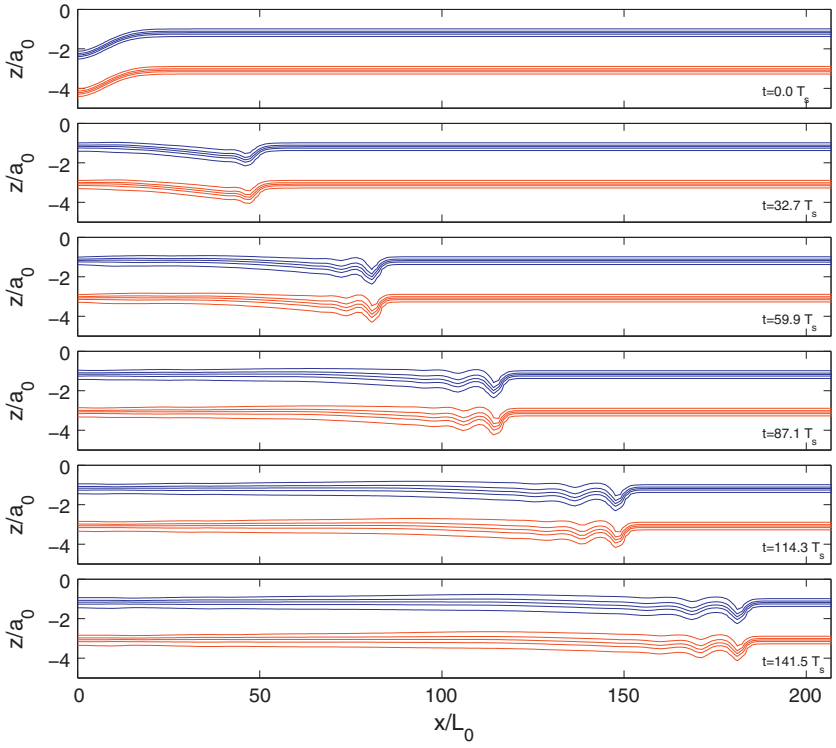

Fig. 7. Comparison of the evolution of a solitary-like internal gravity wave train as computed by SUNTANS with $N_x \times N_z = 150 \times 100$ grid cells ($\lambda = \Delta x/h_1 = 8$) with (upper blue contours) and without (lower red contours) the nonhydrostatic pressure. The horizontal distance is normalized by $L_w = L_0 = 1436$ m, the width of the leading nonhydrostatic wave that is computed with $N_x = 4800$ grid cells at the end of the simulation, and $T_s = L_w/c_0$ is the wave propagation time scale. Density contours are shown for $\rho/\rho_0 = (-0.4, -0.2, 0, 0.2, 0.4)\Delta\rho/\rho_0$. (For interpretation of the references to colour in this figure legend, the reader is referred to the web version of this article.)

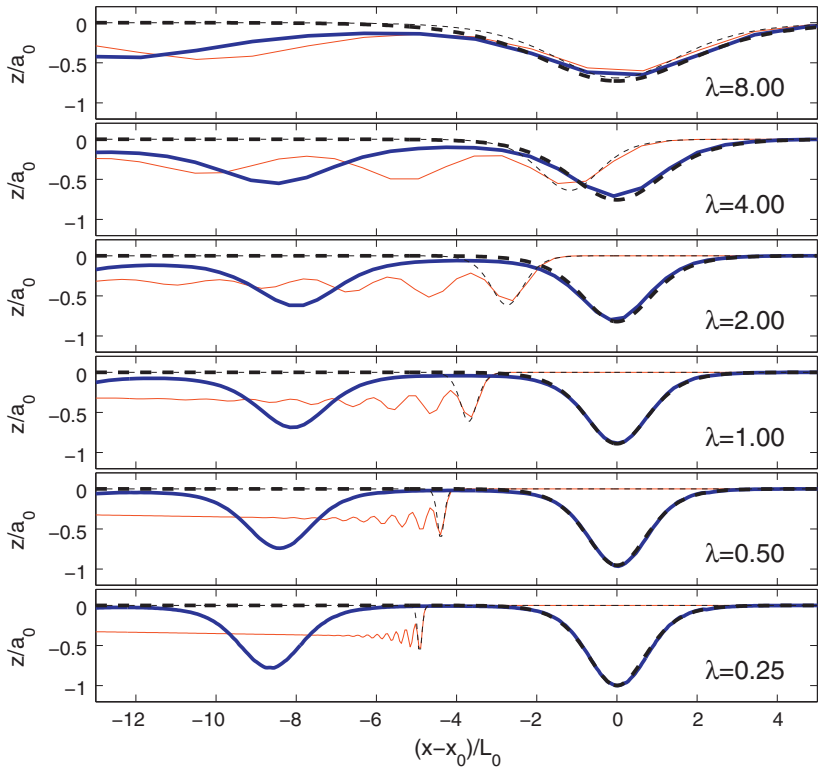

Fig. 8. Effect of grid lepticity $\lambda = \Delta x/h_1$ on the leading solitary-like waves (centered at x_0) in the wave packets as computed by the hydrostatic (faint solid red lines) and nonhydrostatic (thick solid blue lines) SUNTANS models (these are the $\rho = \rho_0$ isopycnals at $t = 141.5\ T_s$). The thin dotted line is the best-fit leading soliton for the hydrostatic result, while the thick dashed line is that for the nonhydrostatic result. The results are normalized by the analytical soliton length scale $L_0 = 1436$ m. (For interpretation of the references to colour in this figure legend, the reader is referred to the web version of this article.)

3.3. Numerical dispersion and the scaling of solitary wave widths

As mentioned previously, the widths of simulated solitons are a good indicator of the magnitude of dispersion. Returning to the form of the numerical soliton given in Eqs. (48) and (49), we see that the simulated soliton scale of a second-order accurate nonhydrostatic model relative to the analytical soliton scale is given by $L/L_0 = L^*/L_0^* = \sqrt{1+\Gamma} = \sqrt{1+K\lambda^2}$. Likewise, for a second-order accurate hydrostatic model, the ratio is given by $L_h/L_0 = L_h^*/L_0^* = \sqrt{\Gamma} = \lambda\sqrt{K}$. In this paper we have highlighted the form of $\Gamma = K\lambda^2 = K(\Delta x^*/\epsilon)^2$. Verification of the correct form of Γ as determined in this paper is possible by comparing the scaling of modeled solitons to the theoretical relationships for the hydrostatic and nonhydrostatic simulations, respectively, as the grid lepticity increases. This analysis is shown in Fig. 9 for the KdV equation and Fig. 10 for the SUNTANS model.

The analysis in Fig. 9 uses the numerical method from Eq. (31), which has $K = 1 - C^2 = 0.9999$, since $C = 0.01$. The simulations are performed with identical conditions to the simulations above in Section 3.1 with $t^*_{\max} = 30$ and a variety of different resolutions, namely $N_x = 1000$, 800, 600, 500, 400, 300, 250, 220, 210, 180, 150, 125, 100, 80, 60, 50, 40, 35, 30, 25. For each simulation, the simulated soliton width, L_{sim}, is calculated as the length from the location of the parabolic maximum, x_0, to the horizontal location, x_c, (on the right) where the soliton obtains an amplitude of $a\text{sech}^2(1)$. This length scale $L_{sim} = x_c - x_0$ corresponds approximately to half of the 42%-width. The horizontal location, x_c, is determined by fitting a quadratic polynomial to the three points nearest to the soliton peak and inverting the location.

As shown in Fig. 9, the computed soliton widths compare very well with the theoretically-expected soliton widths. The close agreement is particularly notable for small values of the grid lepticity, that is for $\lambda < O(1)$. The agreement is not as good for $\lambda > O(1)$ because the theoretical relationships assume 1st-order numerical dispersion. For $\lambda > O(1)$, higher-order numerical dispersion also affects the soliton length scales. Even with the deviations due to higher-order effects when $\lambda > O(1)$, the agreement of the

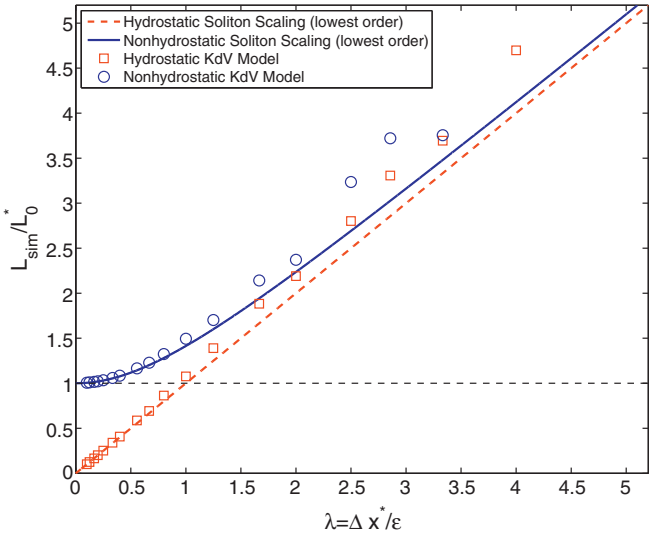

Fig. 9. The relationship between the grid lepticity, λ, and the deviation from the theoretical soliton length scales for the KdV equation. The theoretical prediction for the model performance is $L_{sim}/L_0^* = L^*/L_0^* = \sqrt{1+K\lambda^2}$ for the nonhydrostatic model (solid blue line) and $L_{sim}/L_0^* = L_h^*/L_0^* = \lambda\sqrt{K}$ for the hydrostatic model (dashed red line) where $K = 0.9999$. (For interpretation of the references to colour in this figure legend, the reader is referred to the web version of this article.)

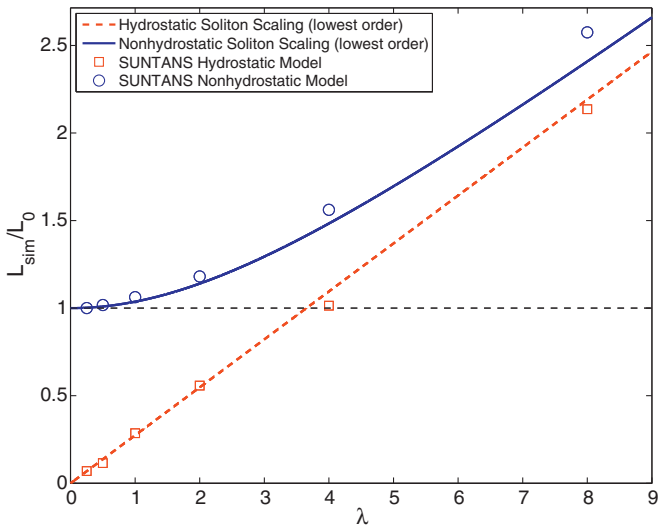

Fig. 10. The relationship between the grid lepticity, λ, and the soliton length scale, L_{sim}/L_0 for the SUNTANS model. The theoretical predictions are $L_{sim}/L_0 = L/L_0 = \sqrt{1+K\lambda^2}$ for the nonhydrostatic model (solid blue line) and $L_{sim}/L_0 = L_h/L_0 = \lambda\sqrt{K}$ for the hydrostatic model (dashed red line), where $K = 0.075$. (For interpretation of the references to colour in this figure legend, the reader is referred to the web version of this article.)

models and the theoretically-predicted soliton length scales is quite remarkable.

We test the SUNTANS model to determine the scaling of the soliton widths using the analysis presented in Fig. 9. Fig. 10 shows that the theory for the dependence of the soliton length scale on the grid lepticity (Eqs. (48) and (49)) is valid for the continuously stratified system when simulated with both a hydrostatic and a nonhydrostatic ocean model. The soliton widths are determined using the same method as above for the $\rho = \rho_0$ density contour. The nonhydrostatic SUNTANS model computes solitons with $L_{sim}/L_0 \approx \sqrt{1+K\lambda^2}$, while the hydrostatic SUNTANS model computes solitons with $L_{sim}/L_0 \approx \lambda\sqrt{K}$, where $K = 0.075$ as obtained with a least-squares fit (L_{sim} is computed using the same technique as that for the KdV simulations).

4. Discussion

For weakly nonlinear, weakly nonhydrostatic waves, discretization of the linear problem, that is, acceleration balancing a pressure gradient, gives rise to most of the numerical dispersion. For weakly nonhydrostatic waves, water wave theory gives the lowest-order physical dispersion as proportional to $(k\epsilon)^2$. The numerical discretization of the linear problem using second-order, central finite-differencing produces, to lowest order, numerical dispersion proportional to $(k\Delta x^*)^2$. The ratio of these two effects is the ratio of numerical to physical dispersion, Γ, which is proportional to the grid lepticity squared, viz. $\Gamma = K\lambda^2$, where K is typically an $O(1)$ constant. Scotti and Mitran (2008) showed that the nonlinear advection term introduces an artificial term in the dispersion relation of magnitude $O(\delta\lambda^2)$. However, we have shown that the discretization of the linear problem and not the nonlinear advection term is responsible for the dominant source of dispersion for weakly nonlinear, weakly nonhydrostatic waves. The relative magnitudes of the numerically dispersive effects of the linear problem vs. the nonlinear advection problem depend on the relative magnitudes of K and δ. Typically $K = O(1)$ and $\delta \ll O(1)$ due to the weakly nonlinear scaling of most oceanic problems of interest. Thus the numerical dispersion induced by the linear term is typically one order of magnitude larger than the numerical dispersion induced by the nonlinear advection term. Highly nonlinear and nonhydrostatic (i.e. $\delta \approx \epsilon^2 = O(1)$) dynamical problems in the ocean are important but confined to small-scale turbulent motions. In modeling such situations, the dispersive error from nonlinear advection terms with magnitude $O(\delta\lambda^2)$ may exceed the dispersive error from the linear terms with magnitude $O(K\lambda^2)$. Thus ensuring small values of the grid lepticity, λ, may be even more important in such cases. Typically, in highly nonlinear problems the motion is governed by a balance between nonlinear advection and the nonhydrostatic pressure gradient. Large-eddy-simulation (LES) is the preferred approach under such circumstances. LES models seek to minimize the numerical dissipation to capture the correct turbulent dissipation. Ocean models, on the other hand, should seek to minimize numerical dispersion, particularly when modeling wave phenomena. For internal wave simulations, the dominant source of numerical dispersion arises from the discretization of the baroclinic pressure gradient. For surface wave simulations (i.e. tsunami modeling), the dominant source of numerical dispersion is the discretization of the barotropic pressure gradient.

When $\Gamma \gg 1$, or when the grid lepticity is large, i.e. $\lambda > O(1)$, simulations produce an overly dispersive result because the physical dispersion is negligible in comparison to the numerical dispersion. This implies that a nonhydrostatic simulation is indistinguishable from a hydrostatic simulation when the grid spacing is large relative to the relevant depth scale. Such a large grid spacing may therefore give a false impression that nonhydrostatic physics must be unimportant. Scotti and Mitran (2008) developed an approximated method to reduce the computational cost of computing the nonhydrostatic pressure in thin domains which converges when $\lambda > O(1)$. However, when this condition is satisfied, the solution is contaminated by numerical dispersion and the computational overhead associated with solving the full nonhydrostatic problem is small, as shown in Fig. 4. Elliptic approximation methods must therefore be combined with higher-order discretization techniques which minimize numerical dispersion if they are to be viable.

5. Conclusions

We have determined the magnitude of physical and numerical dispersion coefficients from asymptotic approximations for weakly nonlinear, weakly nonhydrostatic models. The ratio of numerical to physical dispersion, Γ, for nonhydrostatic ocean models that are second-order accurate in time and/or space is given by $\Gamma = K\lambda^2$, where $\lambda \equiv \Delta x/h_1$ is the grid leptic ratio or lepticity, and K is typically an $O(1)$ constant. Simulations of internal waves using the SUNTANS nonhydrostatic ocean model are well-reproduced by the KdV equation, thereby validating its use to quantify the magnitudes of physical and numerical dispersion.

For hydrostatic models, the ratio Γ is infinite because there is no resolved physical dispersion. However, when the leptic ratio is large, numerical simulations based on either hydrostatic or nonhydrostatic models will be dominated by numerical dispersion. For simulations of internal waves, the amount of physical dispersion is critical to resolving the correct behavior, and thus a well-resolved nonhydrostatic model or approximation thereof is required. Numerical solutions of internal waves when modeled with second-order accuracy in time or space will be realistic only when $\lambda < O(1)$ or $\Delta x < h_1$. The relationship $\Gamma = K\lambda^2$ is primarily due to the second-order accurate discretization of the baroclinic pressure gradient. The severity of this condition may be loosened using higher-order differencing schemes or schemes with better dispersive properties such as Padé schemes (Lele, 1992). Adaptive mesh refinement (AMR) methods, which allow additional resolution when necessary, also present a possible solution.

The condition that $\lambda < O(1)$, or $\Delta x < h_1$, is consistent with the scaling of nonhydrostatic effects, since they occur when vertical scales of motion are roughly equal to the horizontal scales. Therefore, accurate simulation of nonhydrostatic effects requires that horizontal scales of $O(h_1)$ must be resolved. This constraint may be a significant additional resolution requirement beyond the current state-of-the-art in ocean modeling.

Acknowledgments

Sean Vitousek gratefully acknowledges his support as a DOE Computational Science Graduate Fellow. Sean Vitousek and Oliver B. Fringer gratefully acknowledge the support of ONR as part of the YIP and PECASE awards under grants N00014-10-1-0521 and N00014-08-1-0904 (scientific officers Dr. C. Linwood Vincent, Dr. Terri Paluszkiewicz and Dr. Scott Harper). We thank Alberto Scotti for numerous discussions which contributed to the ideas in this manuscript. We also thank two anonymous reviewers for their comments and suggestions which led to a significant improvement of the manuscript.

Appendix A. Modified equivalent partial differential equation analysis

We show how the modified equivalent partial differential equation (MEPDE) (34) of the discretization (31) is obtained. MEPDE analysis begins with the expansion of the adjacent grid points in Taylor series usually about the central point. In this case these expansions are given by

$$\xi^n_{i+1} = \xi^n_i + \Delta x^* \left.\frac{\partial \xi^*}{\partial x^*}\right|^n_i + \frac{(\Delta x^*)^2}{2}\left.\frac{\partial^2 \xi^*}{\partial x^{*2}}\right|^n_i + \frac{(\Delta x^*)^3}{6}\left.\frac{\partial^3 \xi^*}{\partial x^{*3}}\right|^n_i + \cdots \tag{A.1}$$

$$\xi^n_{i-1} = \xi^n_i - \Delta x^* \left.\frac{\partial \xi^*}{\partial x^*}\right|^n_i + \frac{(\Delta x^*)^2}{2}\left.\frac{\partial^2 \xi^*}{\partial x^{*2}}\right|^n_i - \frac{(\Delta x^*)^3}{6}\left.\frac{\partial^3 \xi^*}{\partial x^{*3}}\right|^n_i + \cdots \tag{A.2}$$

$$\xi^n_{i+2} = \xi^n_i + 2\Delta x^* \left.\frac{\partial \xi^*}{\partial x^*}\right|^n_i + 2(\Delta x^*)^2 \left.\frac{\partial^2 \xi^*}{\partial x^{*2}}\right|^n_i + \frac{4(\Delta x^*)^3}{3}\left.\frac{\partial^3 \xi^*}{\partial x^{*3}}\right|^n_i + \cdots \tag{A.3}$$

$$\xi^n_{i-2} = \xi^n_i - 2\Delta x^* \left.\frac{\partial \xi^*}{\partial x^*}\right|^n_i + 2(\Delta x^*)^2 \left.\frac{\partial^2 \xi^*}{\partial x^{*2}}\right|^n_i - \frac{4(\Delta x^*)^3}{3}\left.\frac{\partial^3 \xi^*}{\partial x^{*3}}\right|^n_i + \cdots, \tag{A.4}$$

where, $\xi^n_i = \xi^*(x^*_i, t^*_n) = \xi^*(i\Delta x^*, n\Delta t^*)$. Using these expressions, the form of the truncation error of the second-order, central finite-difference approximation to the spatial derivative is given in Eq. (32). Similarly, the truncation error for the second-order, leap-frog time derivative is given by

$$\frac{\xi^{n+1}_i - \xi^{n-1}_i}{2\Delta t^*} = \left.\frac{\partial \xi^*}{\partial t^*}\right|^n_i + \frac{(\Delta t^*)^2}{6}\left.\frac{\partial^3 \xi^*}{\partial t^{*3}}\right|^n_i + \frac{(\Delta t^*)^4}{120}\left.\frac{\partial^5 \xi^*}{\partial t^{*5}}\right|^n_i + \frac{(\Delta t^*)^6}{5040}\left.\frac{\partial^7 \xi^*}{\partial t^{*7}}\right|^n_i + O\left((\Delta t^*)^8\right). \tag{A.5}$$

The second-order accurate, centered 3rd-order spatial derivative is given by

$$\frac{\frac{1}{2}\xi^n_{i+2} - \xi^n_{i+1} + \xi^n_{i-1} - \frac{1}{2}\xi^n_{i-2}}{(\Delta x^*)^3} = \left.\frac{\partial^3 \xi^*}{\partial x^{*3}}\right|^n_i + \frac{(\Delta x^*)^2}{4}\left.\frac{\partial^5 \xi^*}{\partial x^{*5}}\right|^n_i + O\left((\Delta x^*)^6\right). \tag{A.6}$$

Substitution of Eqs. (32), (A.5), and (A.6) into the complete discretization (31) gives:

$$\left.\frac{\partial \xi^*}{\partial t^*}\right|^n_i + \frac{(\Delta t^*)^2}{6}\left.\frac{\partial^3 \xi^*}{\partial t^{*3}}\right|^n_i + \left(1 - \frac{3}{2}\delta\xi^n_i\right)\left(\left.\frac{\partial \xi^*}{\partial x^*}\right|^n_i + \frac{(\Delta x^*)^2}{6}\left.\frac{\partial^3 \xi^*}{\partial x^{*3}}\right|^n_i\right) + \frac{\epsilon^2}{6}\left(\left.\frac{\partial^3 \xi^*}{\partial x^{*3}}\right|^n_i + \frac{(\Delta x^*)^2}{4}\left.\frac{\partial^5 \xi^*}{\partial x^{*5}}\right|^n_i\right) = O\left((\Delta x^*)^4, (\Delta t^*)^4\right). \tag{A.7}$$

Since each term is at time level n and spatial index i, and this equation holds for all space and time, we can remove the subscripts and write Eq. (A.7) as:

$$\left[\frac{\partial \xi^*}{\partial t^*} + \left(1 - \frac{3}{2}\delta\xi^*\right)\frac{\partial \xi^*}{\partial x^*} + \frac{\epsilon^2}{6}\frac{\partial^3 \xi^*}{\partial x^{*3}}\right] + \left[\frac{(\Delta t^*)^2}{6}\frac{\partial^3 \xi^*}{\partial t^{*3}} + \left(1 - \frac{3}{2}\delta\xi^*\right)\frac{(\Delta x^*)^2}{6}\frac{\partial^3 \xi^*}{\partial x^{*3}} + \frac{\epsilon^2(\Delta x^*)^2}{24}\frac{\partial^5 \xi^*}{\partial x^{*5}}\right] = O\left((\Delta x^*)^4, (\Delta t^*)^4\right), \tag{A.8}$$

where the first set of bracketed terms represents the terms in the original PDE and the second set of bracketed terms represents the additional terms in the MEPDE that result from the discretization. Recalling that $O(\delta) = O(\epsilon^2) < 1$, Eq. (A.8) can be written as:

$$\left[\frac{\partial \xi^*}{\partial t^*} + \left(1 - \frac{3}{2}\delta\xi^*\right)\frac{\partial \xi^*}{\partial x^*} + \frac{\epsilon^2}{6}\frac{\partial^3 \xi^*}{\partial x^{*3}}\right] + \left[\frac{(\Delta t^*)^2}{6}\frac{\partial^3 \xi^*}{\partial t^{*3}} + \frac{(\Delta x^*)^2}{6}\frac{\partial^3 \xi^*}{\partial x^{*3}}\right] = O\left(\epsilon^2(\Delta x^*)^2, \delta(\Delta x^*)^2, (\Delta x^*)^4, (\Delta t^*)^4\right). \tag{A.9}$$

We ignore the truncation error terms in the MEPDE created from the nonlinear advection and dispersion terms because they are approximately one order of magnitude smaller than the terms resulting from the linear problem. Using the first-order, linear relation:

$$\frac{\partial \xi^*}{\partial t^*} = -\frac{\partial \xi^*}{\partial x^*} + O(\epsilon^2, \delta), \tag{A.10}$$

we have, to $O(\epsilon^2, \delta)$:

$$\frac{\partial^2 \xi^*}{\partial t^{*2}} = \frac{\partial^2 \xi^*}{\partial x^{*2}},$$
$$\frac{\partial^3 \xi^*}{\partial t^{*3}} = -\frac{\partial^3 \xi^*}{\partial x^{*3}}.$$

This result generalizes to Eq. (33). Using this relation, we can rewrite Eq. (A.9) as:

$$\left[\frac{\partial \xi^*}{\partial t^*} + \left(1 - \frac{3}{2}\delta\xi^*\right)\frac{\partial \xi^*}{\partial x^*} + \frac{\epsilon^2}{6}\frac{\partial^3 \xi^*}{\partial x^{*3}}\right] + \left[\frac{(\Delta x^*)^2}{6}\frac{\partial^3 \xi^*}{\partial x^{*3}} - \frac{(\Delta t^*)^2}{6}\frac{\partial^3 \xi^*}{\partial x^{*3}}\right] = O\left(\epsilon^2(\Delta x^*)^2, \delta(\Delta x^*)^2, (\Delta x^*)^4, (\Delta t^*)^4\right), \tag{A.11}$$

or:

$$\left[\frac{\partial \xi^*}{\partial t^*} + \left(1 - \frac{3}{2}\delta\xi^*\right)\frac{\partial \xi^*}{\partial x^*} + \frac{\epsilon^2}{6}\frac{\partial^3 \xi^*}{\partial x^{*3}}\right] + \left[\left(1 - C^2\right)\frac{(\Delta x^*)^2}{6}\frac{\partial^3 \xi^*}{\partial x^{*3}}\right] = O\left(\epsilon^2(\Delta x^*)^2, \delta(\Delta x^*)^2, (\Delta x^*)^4, (\Delta t^*)^4\right), \tag{A.12}$$

where $C \equiv \Delta t^*/\Delta x^*$. This gives the numerical dispersion coefficient $\beta = (1 - C^2)\frac{(\Delta x^*)^2}{6}$ in Eq. (34).

Appendix B. Convergence analysis for the KdV discretization

In this section we perform a grid-refinement convergence analysis of the discrete KdV equation (31) to verify that the numerical method is indeed second-order accurate. Fig. B.11 shows that the centered finite-difference method given in Eq. (31) is second-order accurate in time. The temporal convergence analysis shown in Fig. B.11 is performed for the evolution of an initial Gaussian hump

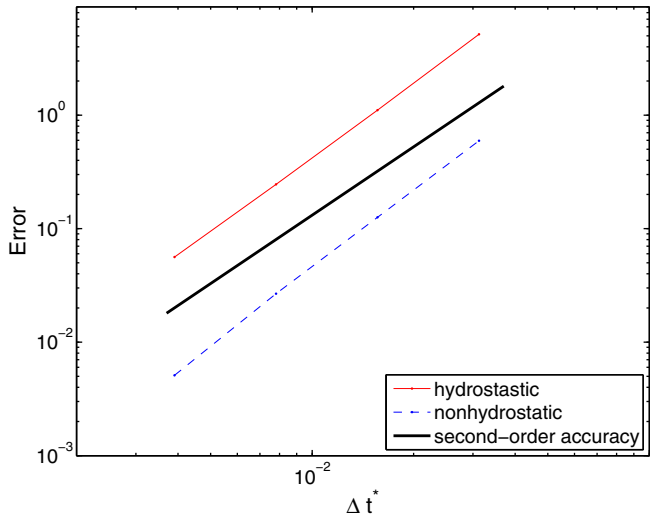

Fig. B.11. Temporal convergence of the numerical KdV solution given in Eq. (31). The convergence analysis shows that all methods converge with second-order accuracy, $O((\Delta t^*)^2)$, with refinement of the time step size, Δt^*.

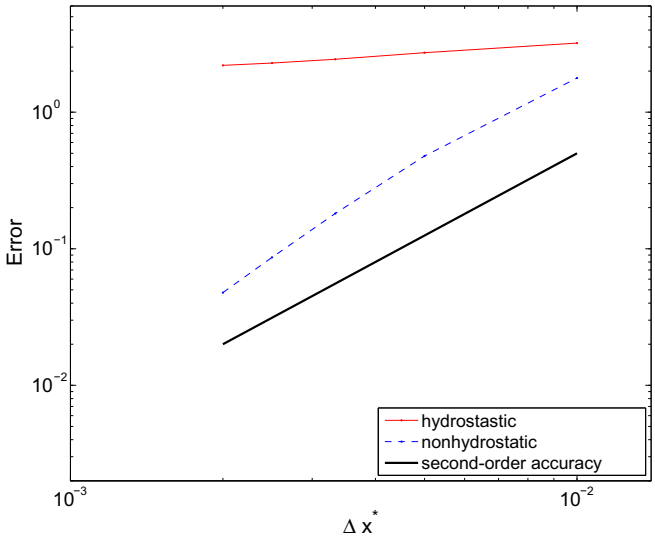

Fig. B.12. Spatial convergence of the numerical KdV solution given in Eq. (31).

of the form given in Eq. (50), with identical parameters as in Section 3.1, on a grid with $N_x = 200$ grid points and with a Courant number $C = \frac{\Delta t^*}{\Delta x^*}$, for various time step sizes $\Delta t^* = 1/512, 1/256, 1/128, 1/64, 1/32$ with $t^*_{\max} = 10$. Recall that the $*$ notation refers to nondimensional variables. The measure of convergence of the solution (Figs. B.11, B.12) is obtained by: Error = $\|$ solution (Δx^* or Δt^*) – solution ($\Delta x^*/2$ or $\Delta t^*/2$)$\|_2$, where "solution" means the numerical solution of ξ^* on a grid of size Δx^* or with a time step of Δt^*. As shown in Fig. B.11, the numerical solution obtains $O((\Delta t^*)^2)$ convergence, as expected.

Convergence with respect to spatial resolution is shown in Fig. B.12. This analysis is performed for identical initial conditions as the temporal convergence analysis, with grid spacing given by $\Delta x^* = 1/600, 1/500, 1/400, 1/300, 1/200, 1/100$. Each simulation is performed with a time step of $\Delta t^* = 0.00005$ and with $t^*_{\max} = 5$. The measure of convergence of the solution is obtained using the method explained above. The coarse-grid solution is interpolated onto the highest resolution domain using a cubic-spline interpolation method and the norm of the difference between the solutions at various resolutions provides the measure of convergence.

Unlike the temporal convergence, spatial convergence is not as well-behaved. The nonhydrostatic method, as shown in Fig. B.12, converges with spatial-refinement with approximately second-order accuracy. However, the hydrostatic model does not converge with spatial-refinement. Lack of convergence results from the magnitude of (numerical) dispersion which is a function of Δx^*. Therefore, numerical solitons appear with increasingly smaller widths that are always proportional to the grid spacing via Eq. (46). The lack of convergence is a common problem arising from invalid assumptions of hydrostatic models. For example, when calculating a lock-exchange flow, Fringer et al. (2006) show that the hydrostatic model yields exceedingly large vertical velocities. This occurs because of the ill-posedness of the hydrostatic model which causes an inverse dependence of the vertical velocity on Δx. Horizontal grid refinement leads to unbounded increase in the vertical velocity when a hydrostatic model is used to simulate an inherently nonhydrostatic problem.

References

Apel, J., Holbrook, J., Liu, A., Tsai, J., 1985. The Sulu Sea internal soliton experiment. J. Phys. Oceanogr. 15, 1625–1651.

Asselin, R., 1972. Frequency filter for time integrations. Mon. Weather Rev. 100, 487–490.

Bleck, R., Rooth, C., Hu, D., Smith, L.T., 1992. Salinity-driven thermocline transients in a wind- and thermohaline-forced isopycnic coordinate model of the North Atlantic. J. Phys. Oceanogr. 22, 1486–1505.

Blumberg, A.F., Mellor, G.L., 1987. A description of a three-dimensional coastal ocean circulation model. In: Heaps, N. (Ed.), Three-Dimensional Coastal Ocean Models. American Geophysical Union, pp. 1–16.

Boussinesq, J., 1871. Thorie de l'intumescence liquide, applele onde solitaire ou de translation, se propageant dans un canal rectangulaire. C.R. Acad. Sci. 72, 755759.

Boussinesq, J., 1872. Thorie des ondes et des remous qui se propagent le long d'un canal rectangulaire horizontal, en communiquant au liquide contenu dans ce canal des vitesses sensiblement pareilles de la surface au fond. J. Math. Pure Appl. 17, 55108.

Burwell, D., Tolkova, E., Chawla, A., 2007. Diffusion and dispersion characterization of a numerical tsunami model. Ocean Modell. 19, 10–30.

Casulli, V., Cattani, E., 1994. Stability, accuracy and efficiency of a semi-implicit method for three-dimensional shallow water flow. Comput. Math. Appl. 27, 99–112.

Cushman-Roisin, B., Beckers, J., 2010. Introduction to Geophysical Fluid Dynamics: Physical and Numerical Aspects. Academic Press.

Duda, T.F., Lynch, J.F., Beardsley, R.C., Irish, J.D., Ramp, S.R., Chiu, C.S., Tang, T.Y., Yang, Y.J., 2004. Internal tide and nonlinear internal wave behavior at the continental slope in the Northern South China Sea. IEEE J. Ocean. Eng. 29, 1105–1130.

Fringer, O.B., Street, R.L., 2003. The dynamics of breaking progressive interfacial waves. J. Fluid Mech. 494, 319–353.

Fringer, O.B., Gerritsen, M., Street, R.L., 2006. An unstructured-grid, finite-volume, nonhydrostatic, parallel coastal ocean simulator. Ocean Modell. 14, 139–173.

Gottwald, G., 2007. Dispersive regularizations and numerical discretizations for the inviscid burgers equation. J. Phys. A. Math. Theor. 40, 14745.

Grimshaw, R., 2007. Solitary Waves in Fluids. WIT Press, Boston.

Helfrich, K.R., Melville, W.K., 2006. Long nonlinear internal waves. Annu. Rev. Fluid Mech. 38, 395–425.

Hirt, C., 1968. Heuristic stability theory for finite-difference equations. J. Comput. Phys. 2, 335–339.

Hodges, B., Laval, B., Wadzuk, B., 2006. Numerical error assessment and a temporal horizon for internal waves in a hydrostatic model. Ocean Modell. 13, 44–64.

Hunkins, K., Fliegel, M., 1973. Internal undular surges in Seneca Lake: A natural occurrence of solitons. J. Geophys. Res. 78, 539–548.

Kanarska, Y., Shchepetkin, A., McWilliams, J., 2007. Algorithm for non-hydrostatic dynamics in the regional oceanic modeling system. Ocean Modell. 18, 143–174.

Kantha, L., Clayson, C., 2000. Numerical Models of Oceans and Oceanic Processes. Academic Press.

Korteweg, D., de-Vries, G., 1895. On the change of form of long waves advancing in a rectangular canal, and on a new type of long stationary waves. Philos. Mag. 39, 422–443.

LeBlond, P., Mysak, L., 1978. Waves in the Ocean. Elsevier, Amsterdam, The Netherlands.

Lele, S., 1992. Compact finite difference schemes with spectral-like resolution. J. Comput. Phys. 103, 16–42.

Liu, A.K., 1988. Analysis of nonlinear internal waves in the New York Bight. J. Geophys. Res. 93, 12317–12329.

Liu, A.K., Yang, Y.S., Hsu, M.K., Liang, N.K., 1998. Evolution of nonlinear internal waves in the East and South China Seas. J. Geophys. Res. 103, 7995–8008.
Lynett, P.J., Liu, P.L.F., 2002. A two-dimensional, depth-integrated model for internal wave propagation over variable bathymetry. Wave Motion 36, 221–240.
Marshall, J., Adcroft, A., Hill, C., Perelman, L., Heisey, C., 1997. A finite-volume, incompressible Navier Stokes model for studies of the ocean on parallel computers. J. Geophys. Res. 102, 5753–5766.
Marshall, J., Hill, C., Perelman, L., Adcroft, A., 1997. Hydrostatic, quasi-hydrostatic, and nonhydrostatic ocean modeling. J. Geophys. Res. 102, 5733–5752.
Mei, C., 1983. Theory and Applications of Ocean Surface Waves. World Scientific, Singapore.
Pacanowski, R., Griffes, S., 1999. The MOM 3 Manual. Geophysical Fluid Dynamics Laboratory/NOAA, Princeton.
Peregrine, D., 1967. Long waves on a beach. J. Fluid Mech. 27, 815–827.
Schroeder, G., Schlünzen, K., 2009. Numerical dispersion of gravity waves. Mon. Weather Rev. 137, 4344–4354.
Scotti, A., Mitran, S., 2008. An approximated method for the solution of elliptic problems in thin domains: Application to nonlinear internal waves. Ocean Modell. 25, 144–153.
Scotti, A., Pineda, J., 2004. Observations of very large and steep internal waves of elevation near the Massachussetts coast. Geophys. Res. Lett. 31, L22307.
Shchepetkin, A., McWilliams, J., 2003. A method for computing horizontal pressure-gradient force in an oceanic model with a non-aligned vertical coordinate. J. Geophys. Res. 108.
Shuto, N., 1991. Numerical simulation of tsunamis its present and near future. Nat. Hazards 4, 171–191.
Stanton, T.P., Ostrovsky, L.A., 1998. Observations of highly nonlinear internal solitons over the continental shelf. Geophys. Res. Lett. 25, 2695–2698.
Tam, C., Webb, J., 1993. Dispersion–relation–preserving finite difference schemes for computational acoustics. J. Comput. Phys. 107, 262–281.
Trefethen, L.N., 1982. Group velocity in finite difference schemes. SIAM Rev. 24, 113–136.
Vichnevetsky, R., 1980. Propagation properties of semi-discretizations of hyperbolic equations. Math. Comput. Simulat. 22, 98–102.
Vichnevetsky, R., Bowles, J., 1982. Fourier Analysis of Numerical Approximations of Hyperbolic Equations. SIAM.
Wadzuk, B.M., Hodges, B.R., 2009. Hydrostatic versus nonhydrostatic Euler-equation modeling of nonlinear internal waves. J. Eng. Mech. 135, 1069–1080.
Warn-Varnas, A., Hawkins, J., Lamb, K., Piacsek, S., Chin-Bing, S., King, D., Burgos, G., 2010. Solitary wave generation dynamics at Luzon Strait. Ocean Modell. 31, 9–27.
Whitham, G., 1974. Linear and Nonlinear Waves. Wiley-Interscience, New York.
Zauderer, E., 1989. Partial Differential Equations of Applied Mathematics. Wiley, New York.
Zhang, Z., Fringer, O.B., Ramp, S.R., 2011. Three-dimensional, nonhydrostatic numerical simulation of nonlinear internal wave generation and propagation in the South China Sea. J. Geophys. Res. 116, C05022. doi:10.1029/2010JC006424.